University of South-Eastern Norway
Faculty of Technology, Natural Sciences and Maritime Sciences

Master's Thesis

Study programme: Master of Science in Micro and Nano Systems Technology

Spring/Autumn 2023

Hamza Ahmed

Optimized Ni Nanoparticle Deposition for iCL-CNT Growth for High Energy Density Supercapacitors

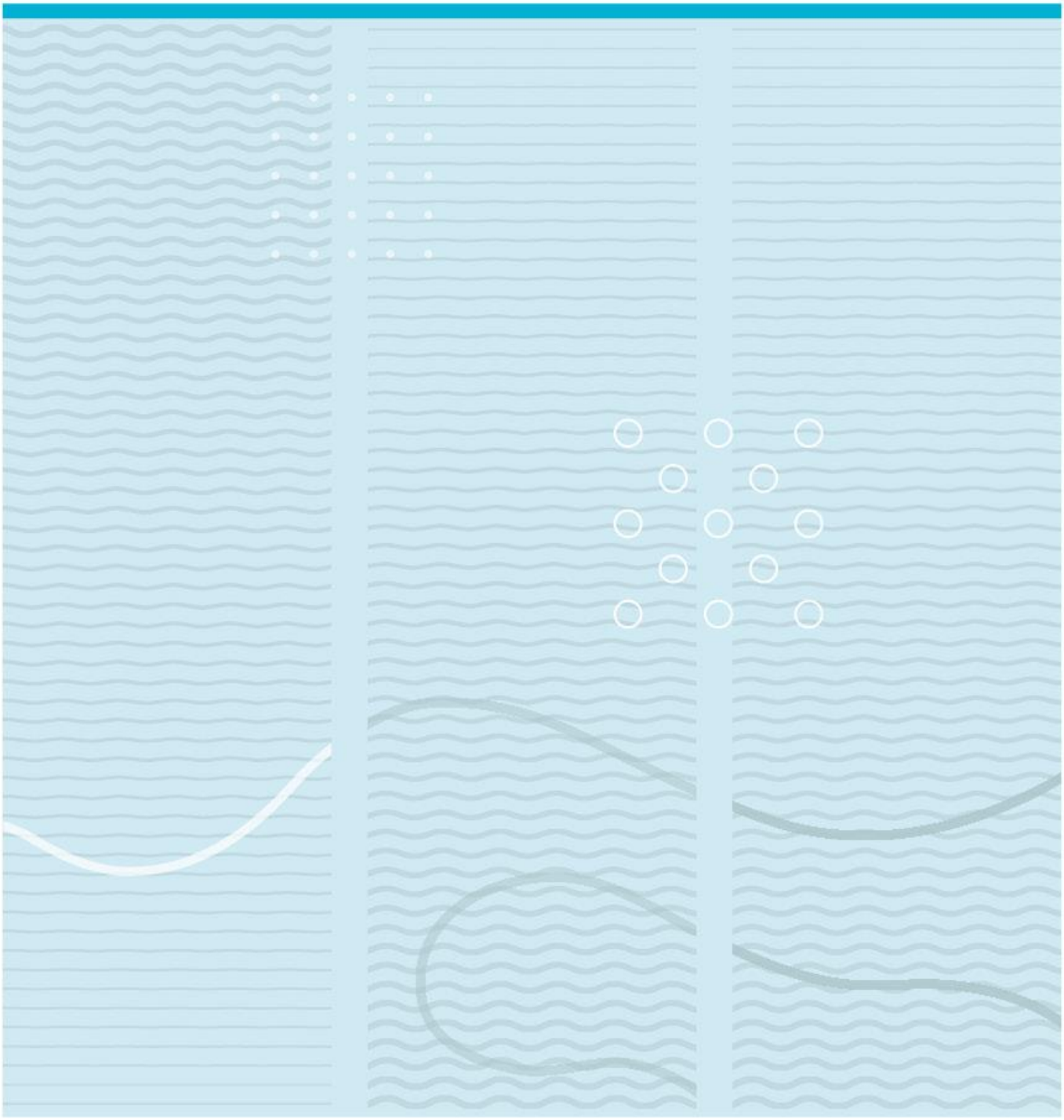

University of South-Eastern Norway
Faculty of Technology, Natural Sciences and Maritime Sciences
Department of Microsystems.
Raveien 215
NO-3184 Borre, Norway

http://www.usn.no

Summary

This thesis investigates the effect of different sputter deposition parameters on the diameter, morphology, and distribution of nickel nanoparticles, and the consequently synthesized interconnected cross-linked carbon nanotubes (iCL-CNTs) for high energy density supercapacitors. Ni is a metal catalyst with excellent properties for CNT synthesis, which is sputter-deposited on a microstructured Al foil substrate (*featuring large surface area*) acting as electrode with CNTs grown on it for supercapacitor application. Since the morphology of Ni nanoparticles has a strong influence on the diameter of the resulting carbon nanotubes, therefore an approach is devised to study this effect and present optimized deposition parameters and conditions for Ni. The supercapacitors suffer from the problem of low energy density, and the thesis presents an approach to improve it.

Ni thin films of 10, 100 and 250 nm are sputter-deposited on a microstructured Al foil at applied powers of 25, 100, and 400 W (*corresponding sputtering rates: 0.14, 0.77, and 3.2 Å/s*) to study the influence of these parameters on the CNT growth. The CNTs were grown using an optimized gas ratio and then their mass loading was calculated. Ni nanoparticles of ~7.76 nm were characterized and CNTs measuring between 30 and 160 nm were grown. The effect of the applied power on the penetration depth of Ni into the microstructured Al substrate was also studied, and higher powers (*sputtering rates*) and thicker films were found to provide a larger Ni concentration or penetration depth.

At the same time, faster sputtering rates and thicker Ni films were found to increase the Ni nanoparticle/cluster size. The coalescence property of nanoparticles and its relationship with heating were studied. CNT mass loading of ~23.7 $\frac{mg}{cm^2}$ was achieved which can then be extrapolated to comment on improvement in the energy density of a supercapacitor.

Acknowledgements

First and foremost, I would like to express my sincere gratitude to everyone who supported me throughout this degree program including lecturers, fellow students, colleagues, and lab engineers. Their constant presence and support provided me the strength and determination to pursue this academic endeavour.

I am immensely grateful to my supervisor, Professor Xuyuan Chen, for his exceptional mentorship, insightful feedback and continuous encouragement throughout my thesis. Having said that, I must also thank my co-supervisor, Professor Per Alfred Øhlckers, who offered thought-provoking discussions and constructive criticism that helped enhance my understanding of the subject matter.

I am indebted to the Chief Technology Researcher at nanoCaps AS, Dr. Ing. Raghunandan Ummethala for his unwavering support, guidance, and mentorship throughout. He has played an integral role in shaping the direction of this research work and I am fortunate to have had the opportunity to work under his guidance.

I would also like to acknowledge Associate Professor, Pai Lu for his continuous support and valuable suggestions. Furthermore, I am grateful to Gaurav Sharma for his willingness to assist me with the characterization of my samples. I appreciate Thai Anh Tuan Nguyen for being available whenever I encountered problems.

Finally, I would like to express my deepest appreciations to my parents, Abdul Hafeez and Sajida Parveen, for their unconditional love and constant encouragement. Their belief in me has been the driving force behind my academic journey, and I am forever grateful for their presence in my life.

Contents

List of Figures

List of Tables

Nomenclature

Symbol	Description
Ni	Nickel
CNT	Carbon Nanotube
iCL-CNT	Interconnected Cross-linked Carbon Nanotube
SC	Supercapacitor
EDLC	Electrochemical Double Layer Capacitor
Al	Aluminum
Si	Silicon
DC	Direct Current
PVD	Physical Vapor Deposition
CVD	Chemical Vapor Deposition
APCVD	Atmospheric Pressure Chemical Vapor Deposition
Ar	Argon
SEM	Scanning Electron Microscope
FESEM	Field Emission Scanning Electron Microscope
EDX	Energy Dispersive X-ray Spectroscopy

1 Introduction

Energy storage devices have played an integral role in the development and progress of our civilization [1], [2]. Since the industrial revolution, the economic prosperity of the nation has been dictated by the massive consumption of fossil fuels as an easily accessible carbon source, such as coal, oil, and gas [3], [4]. According to the World Energy Council, the demand for global energy is predicted to increase by 45%-60% by 2030, and for European Union, it is expected to rise by 15%-20% [5]. In the face of ever-growing demands for electric vehicles and other applications of regenerative energy storage, supercapacitors have been researched extensively in a bid to enhance their energy density. At present, lithium-ion batteries are the major player in the energy storage sector, however, these batteries have a low power density which restricts their use in several integrated power modules. On the other hand, supercapacitor, a state-of-the-art energy device with high power density, fast charge/discharge cycles, long cycle life, and a higher energy density compared to conventional capacitors, is regarded as an energy device exhibiting the ability to fill the power/energy gap between batteries, fuels cells and conventional capacitors. A supercapacitor has high power density (the rate at which energy can be delivered per unit volume or mass) but it suffers from the problems of low energy density. This means that a supercapacitor can store only a relatively small amount of energy per unit volume or mass which is not enough for applications that require high energy storage. This includes electric vehicles and renewable energy storage. It can however be used in combination with a battery to power electrical vehicles as it can provide a short-duration power boost for vehicle acceleration. The supercapacitor can also be used alone for applications such as regenerative braking or as a backup power supply. The supercapacitor uses carbon nanomaterials as electrode materials for which carbon nanotubes (CNTs) are a suitable choice because of their extraordinary large specific surface area, high electric conductivity, mechanical properties, operating temperatures, and enhanced chemical stability [6]–[10]. CNTs are in fact a much better replacement for activated carbons as the latter presents a low specific capacitance due to the presence of many micropores which lowers electrode-electrolyte accessibility [11]. The use of carbon nanotubes as electrode materials in a supercapacitor allows much higher conductivity than other carbonaceous materials, thereby removing complex

designs and paving the way for a non-intricate and lightweight device. Transition metals such as Ni, Fe, and Co are typically used for synthesizing carbon nanotubes using processes such as laser ablation, arc discharge, and chemical vapor deposition (CVD). The properties of carbon nanotubes are largely governed by parameters such as the catalyst material, substrate/current collector, applied power during the catalyst nanoparticles deposition process, substrate temperature, quantity of hydrocarbons, synthesis process duration, and so on. Moreover, the use of gel/liquid electrolytes and thin films containing CNTs is conducive to developing flexible supercapacitors that can be utilized for powering bendable displays and touchpads.

The primary objective of the thesis is to optimize the energy density of the supercapacitor by controlling and optimizing the parameters used for depositing nickel catalyst nanoparticles on a non-planar, microstructured aluminum current collector. There is not much literature dedicated to the study of the effect of sputtering rate (*applied power*) when depositing Ni catalyst nanoparticles on aluminum current collector through the DC magnetron sputtering method, and consequently the dimensions and distribution of the synthesized carbon nanotubes which serve as electrodes for the supercapacitor. The diameter and distribution of these CNTs can significantly influence the energy density and capacitance of the supercapacitor. Similarly, the thesis also attempts to explore the effect of different film thicknesses on the non-planar, microstructured aluminum current collector and the resulting CNTs grown through the chemical vapor deposition process. The thesis also expands on the effect of thermal treatment on the Ni nanoparticles and thin film as the substrate is subjected to high temperatures inside the furnace.

The thesis workflow is presented in Figure 1.

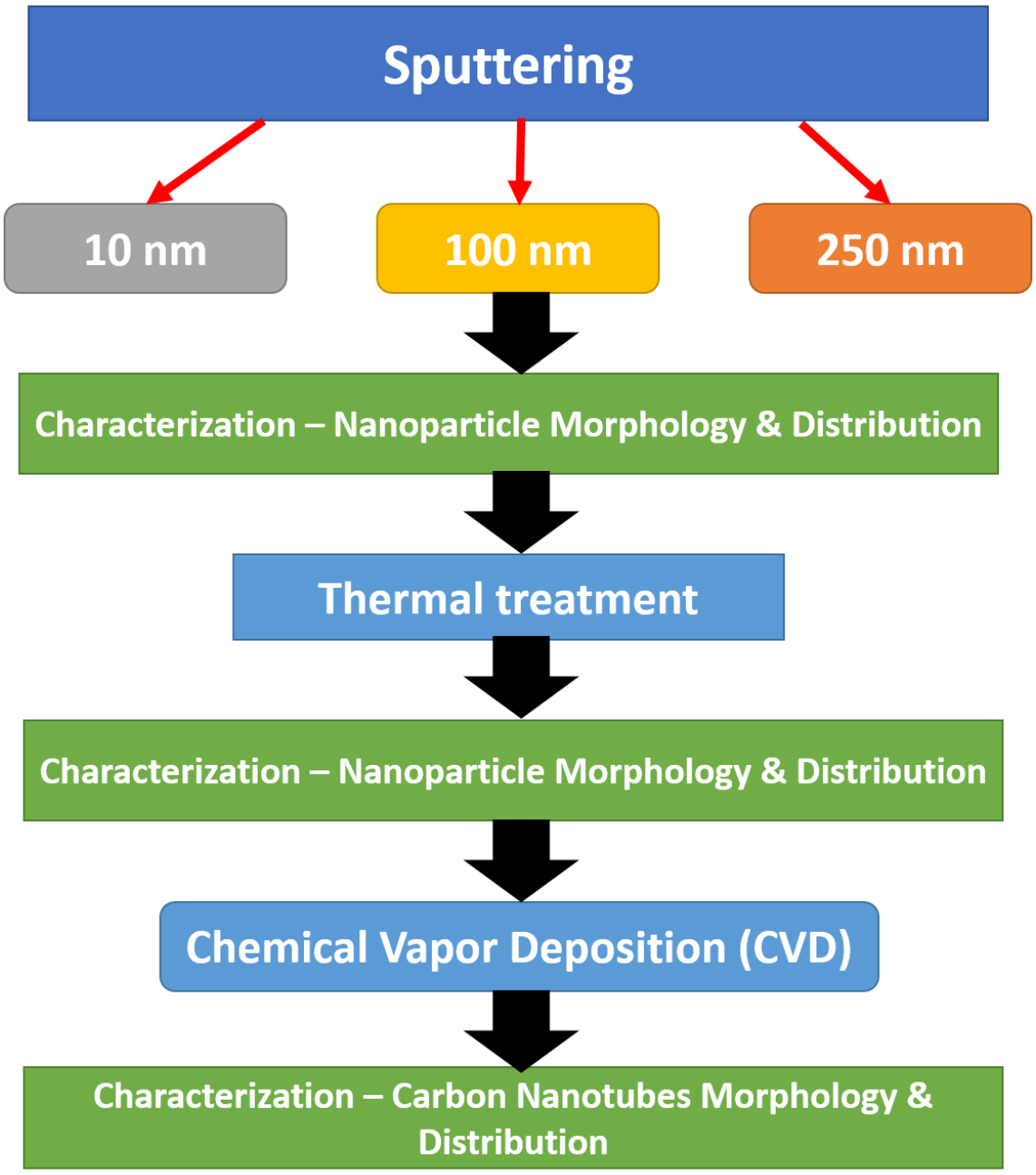

Figure 1: Thesis Workflow

1.1 Scope of Thesis

1.1.1 Research Purpose

As the capacitance and charge storage of a SC is heavily contingent on the electrode materials (carbon nanotubes) therefore, to produce small diameter, interconnected cross-linked carbon nanotubes (iCL-CNTs), certain parameters need to be researched

concerning the physical vapor deposition of the catalyst metal nanoparticles on the current collector (substrate). As it is known that a supercapacitor suffers from the problem of low energy density which means that it cannot store a large amount of energy per unit volume or mass, and hence it is not suitable for high energy storage applications. Therefore, the thesis attempts to enhance the energy density of the supercapacitor. Since the electrode material i.e. carbon nanotube plays an integral role in determining the mass loading and consequently the energy density of the SC, and the CNT itself sprouts from the nanoparticle, therefore the particle size, distribution, and morphology of the Ni nanoparticle can govern the CNT output, and in turn its mass loading and energy density.

1.1.2 Research Approaches

In this thesis, I will attempt to optimize the Ni nanoparticle deposition for interconnected cross-linked carbon nanotubes (iCL-CNTs) growth to develop high energy density supercapacitors. Upon investigation into several physical vapor deposition (PVD) methods, magnetron sputtering is found to be the most suitable for the task at hand. The research approach is to utilize a microstructured aluminum foil (*porous with high surface area*) as the current collector for the SC electrodes. Ni thin films of varying thicknesses are then deposited on the foil using the magnetron sputtering technique at different sputtering rates (*applied powers*) to study their effect on the CNT output. Characterization of the as-deposited Ni particles and thin films is performed to study the size, distribution and morphology of the particles. Then, the substrate with the as-deposited Ni particles will be subjected to heat treatment in a bid to study the transformation a particle experiences during the thermal CVD process. Characterization of the heat-treated sample will be performed to study the effect of heating at high temperatures on Ni particle size, morphology, and distribution. Finally, CNTs will be synthesized and characterized, to study how different thicknesses of the Ni thin films, nanoparticle size, and the powers at which these are deposited on the substrate can influence the shape, diameter, length, and density of the carbon nanotubes.

1.1.3 Thesis Outline

Chapter 2 deals with the theoretical background and the fundamental principles of supercapacitors including electrode materials, catalyst metals, current collectors, carbon nanotubes, sputter deposition technique, and chemical vapor deposition. It also expands on the various important parameters of the sputter equipment for controlling the size, morphology and distribution of the nickel nanoparticle. Furthermore, it discusses the impact of those parameters on the carbon nanotubes and consequently the energy density of the supercapacitor.

Chapter 3 details the experimental setup and methods adapted to carry out the thesis. It expands on the exact parameters, preparations, characterization techniques, calculation methods, as well as modifications that were made to perform the experiments.

Chapter 4 is dedicated to the results and discussion. It details the outcome of the experimentation, and presents an in-depth analysis of the morphology and distribution of Ni nanoparticles, clusters, and carbon nanotubes. It also comments on the influence of applied power on the penetration depth of Ni, the size of the nanoparticles, and the resulting CNT mass loading, which is a crucial determinant of the energy density of the supercapacitor. Furthermore, it presents the results of heat treatment of Ni thin film and the consequences it has on the morphology of Ni nanoparticles.

Chapter 5 presents a conclusion of the entire thesis work as well as recommendations for future work.

2 Theoretical Background

2.1 Supercapacitor in Brief

Supercapacitors, also called electrochemical supercapacitors or ultracapacitors, are unique electrical energy storage devices offering significant advantages over conventional batteries. It is a pulse current system developed to cater to high current and specific powers ($10{,}000WKg^{-1}$) for durations as small as <1 min. Some of their advantages over a battery include fast storage capability (i.e. low discharge time – SC:1-10s vs Li-ion battery: 10-60 min), higher power density, longer cycle life (SC: >30,000h vs battery: >500h) because of their storage mechanism which doesn't involve reversible chemical reactions, and broader operating temperatures (SC: -40 to 100˚C vs battery: -20 to 60˚C) [12], [13]. The electrochemical double layer capacitor (EDLC) has a higher energy density than a traditional capacitor because of its maximum effective surface space and tiny charge separation distances. It uses an electrolyte such as, H_2SO_4, Na_2CO_3 between the electrodes while a capacitor uses a dielectric medium. The principle of charge storage exploits the charging and discharging of the electrochemical double layer (EDL) and physically stores the charges on the electrode surface whilst separating the charge in a Helmholtz double layer between the electrode surface and the electrolyte. One layer of charge is formed as a result of electric voltage on the electrode leads, and to compensate for this, a second ionic layer is formed due to the accumulation of ions of opposing polarity from the electrolyte on the electrodes surface [14]. It is between these two layers the solvent molecules are located. Now since there is a considerable difference in the geometric dimensions of electrons and ions, it leads to a higher density of the electron layer on the electrode surface compared to the second layer. Moreover, there is a linear change in the electrode potential. This unique mechanism of charge accumulation provides for the high charge-discharge cycle rate of a supercapacitor, while at the same time also improving the service life. Additionally, as there are no chemical reactions taking place during the charge-discharge cycle, so the electrode structure remains unaltered. and In order to enhance the capacitance and energy density of supercapacitors, two requirements need to be fulfilled – (i) excellent electrical conductivity to ensure high speed flow of charges during the charging and discharging cycles, (ii) a large surface area to enable a higher number of locations for

charge adherence [15]. A supercapacitor can be used alone or together with another energy storage device such as a battery to provide an overall improved, optimized, and efficient energy and storage solution for several applications including hybrid vehicles, cranes, trains, backup power supplies, windmills, elevators, and electric drives [16], [17].

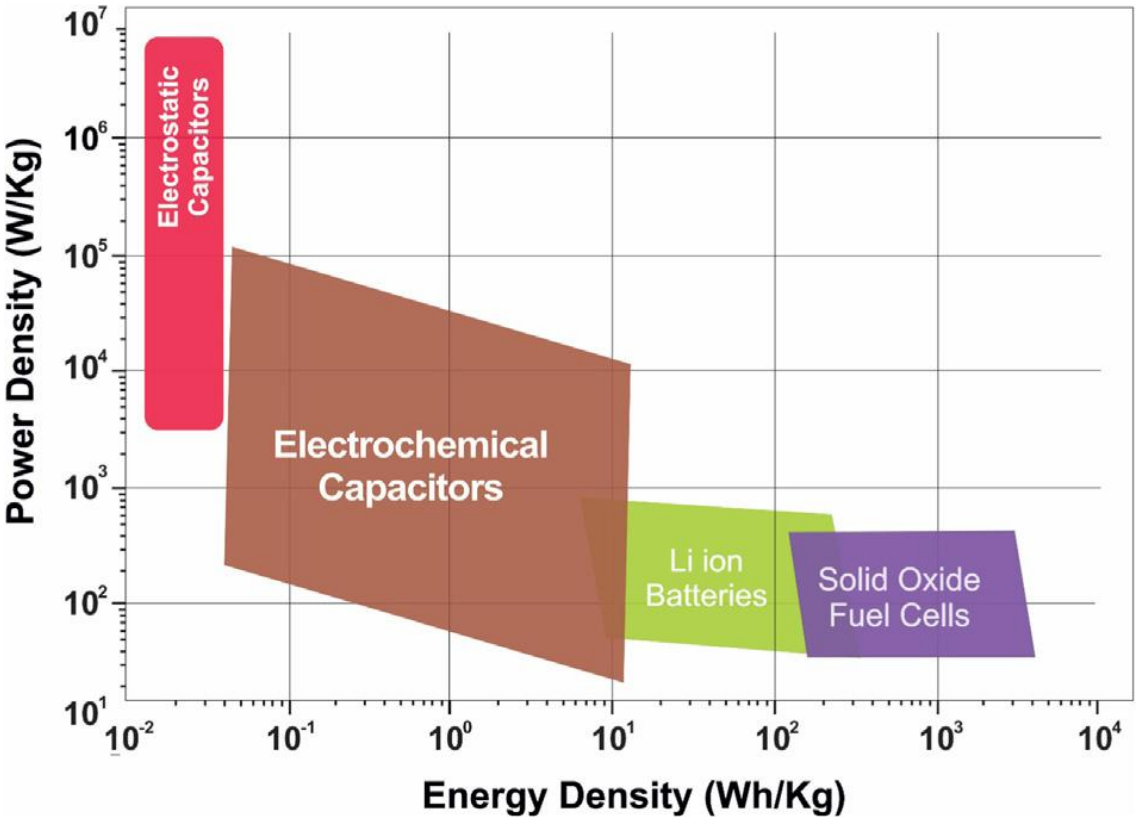

Figure 2: Ragone plots representing energy density vs power density for storage devices such as batteries, fuel cells, and supercapacitors [18].

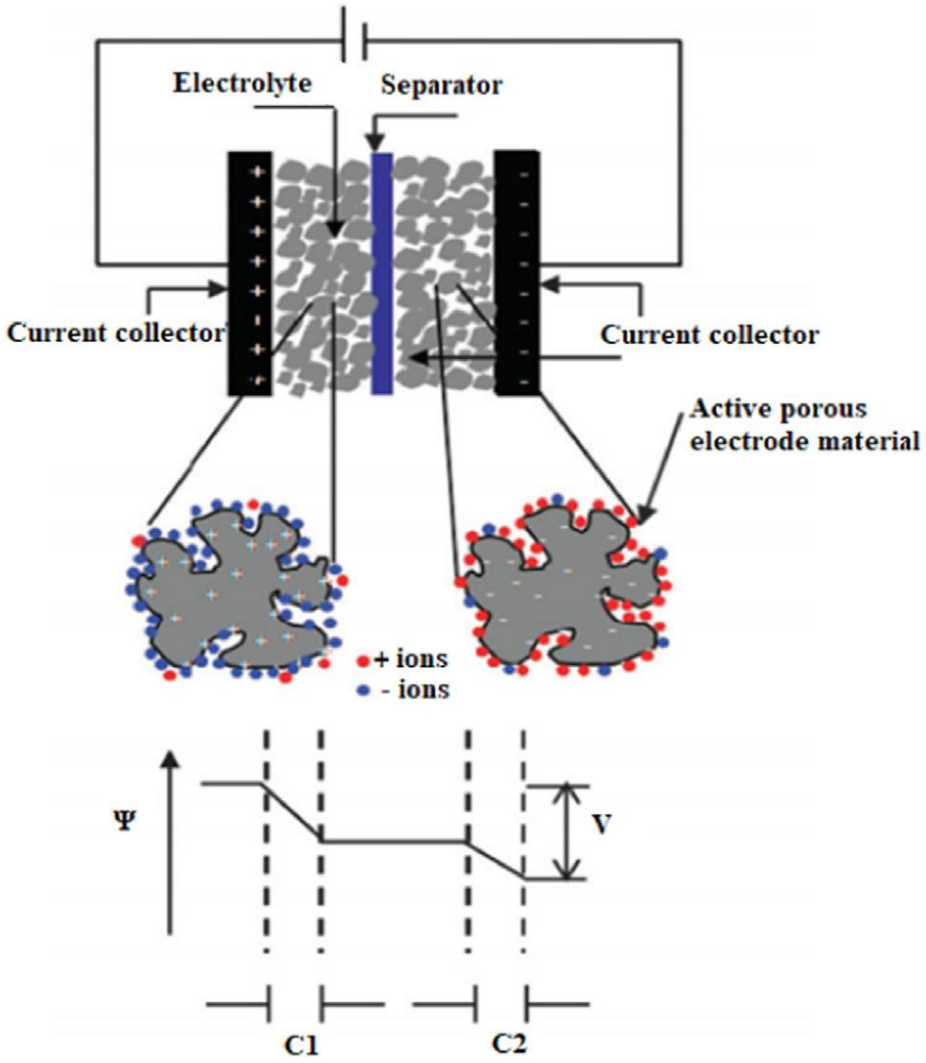

Figure 3: EDLC schematic featuring porous electrodes [19].

2.1.1 Classification of Supercapacitors

The previous section described the EDLCs and their working mechanism in detail. This section deals with the two other types of supercapacitors, (i) Pseudocapacitors and (ii) Hybrid supercapacitors. In the case of pseudocapacitors, the charge accumulation process is called the surface Faradaic electron charge transfer reaction. The electrodes can undergo structural changes in the long run as the reversible reduction and oxidation reactions occur on the electrodes, thus reducing the service life of the pseudocapacitor [20]. This type of supercapacitor is known for high energy density and high capacitance values but low power density compared to EDLCs. Another type is called the hybrid supercapacitor, and as the name suggests, it is made from two different materials.

Similarly, the charge accumulation mechanism also follows a combination of the other two supercapacitor models i.e. the formation of a double electric layer and Faradaic reactions [21]. The hybrid supercapacitor is known for high energy density, reduced self-charging rate and high capacitance.

2.2 Carbon Nanotube (CNT) and its applications for Supercapacitors

The capacitance and charge storage of a supercapacitor are contingent on the electrode materials, and carbon nanotubes (CNTs) provide for a promising material as electrodes. Carbon Nanotubes (CNTs) are graphene sheets rolled up into cylinders. These are known to have diameters as small as one nanometer. First reported by Iijima in 1991 as multi-walled carbon nanotubes (MWCNTs) and two years later as single-walled carbon nanotubes (SWCNTs), this novel material has since then been utilized in several miniaturized electronic, mechanical, electromechanical and other probing devices. A SWCNT is a graphene sheet rolled over into a cylinder while a MWCNT contains concentric cylinders featuring an interlayer spacing. The diameter of SWCNT is smaller, typically of the order of 1.4nm compared to a MWCNT that typically spans 10-20nm in diameter [22].

Interconnected cross-linked carbon nanotubes (iCL-CNTs) feature a structure where CNTs are fused into each other mimicking tunnels that open into one another. This kind of growth allows packing more number of CNTs in a given area compared to vertically aligned CNTs (VACNTs) and consequently, more electrons can flow through them. This leads to higher capacitance and ultimately higher energy density in supercapacitors. Progress in nanotube growth which includes attaining control over several parameters to effectively control the growth of the carbon nanotubes has opened new doors toward future advancement. Their indispensable role in the manufacture of a supercapacitor is one such example. The CNTs are identified as the most suitable candidate for the manufacture of supercapacitors based on their extraordinarily large specific surface area ($1600 m^2 g^{-1}$), electrical conductivity (($105\ S\ cm^{-1}$) [23], porosity, low internal resistance, stability under high current loads, and nanoscale sizes [24]–[26]. CNTs can be synthesized in several ways, with or without a catalyst such as nickel, iron and cobalt,

using a chemical vapor deposition (CVD) process on a variety of different substrates. In terms of supercapacitors, there are two types of CNT electrodes that have been developed so far – (i) binder free, (ii) with binder. The binder-free electrode follows CNTs loosely attached to the current collector which can influence the mechanical stability and the electrical connection. The electrodes created with the binder approach could enable impurities into the electrode with negative consequences for the electrical performance [15].

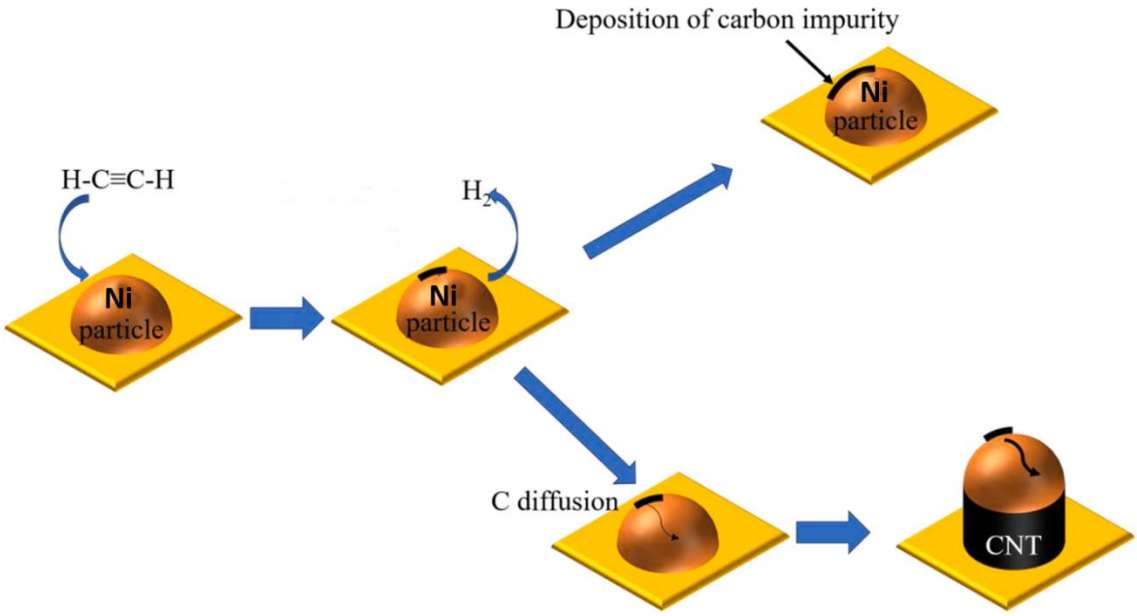

Figure 4: Reproduced schematic representation of CNT growth mechanism from [27].

2.3 Transition Metals as Catalysts for CNT Growth

Transition metals such as Ni, Fe, and Co possess unpaired electrons in their d orbitals, which means that they can both donate and accept electrons based on the reaction. This property makes them highly reactive and able to catalyze the chemical reactions involved in the carbon nanotubes growth. Furthermore, transition metals as catalysts allow greater control over the growth process and the properties of the resulting CNTs. This is because the transition metals can form different phases and sizes of nanoparticles ultimately affecting the diameter and structure of the CNTs grown on them. In addition, transition metals have multiple oxidation states, enabling them to lower the activation energy and accelerate the reaction. Iron (Fe), Nickel (Ni), and Cobalt (Co) are considered the most effective catalysts for CNT synthesis due to their peculiar ability to, (i) catalyze

the decomposition of the carbon source, (ii) manage the reaction and diffusion of carbon intermediates on the surface and within the catalyst particles, (iii) provide a nucleation site for carbon caps, and (iv) keep the sites active for CNT growth [28].

2.3.1 Choice of Nickel as a Catalyst for CNT Growth

Nickel is a ferromagnetic naturally occurring metal abundantly found in the earth's crust. It melts at 1455˚C and is considered a more cost-effective option as a catalyst than most of the other metals [29]. The choice of catalyst can significantly influence the nanotube diameter, growth rate, morphology and microstructure. Ni is one of the most widely used transition metals for synthesizing carbon nanotubes. It reported maximum growth rate of CNTs when Ni was used as a catalyst in comparison with other Fe and Co. The literature suggests the average growth of CNTs on Ni, Co, and Fe is measured as 2±0.3, 1.7±0.3, and 1±0.2 μm/min, respectively. The growth rate is dependent on the carbon diffusion and segregation at the catalyst particle, therefore it can be deduced that carbon should diffuse and segregate on Ni faster than the other transition metals, hence the highest growth rate. It was also found that Fe catalyst particles had the largest diameter and the broadest size distribution (Fe > Co > Ni) before synthesizing CNTs. [30]

Another study performed to evaluate the effect of nickel, iron and cobalt on the growth of aligned carbon nanotubes found that the CNTs catalyzed by Ni possess the best alignment and the smoothest and cleanest wall surface, while those catalyzed from Co had their outer surface contaminated with amorphous carbon and nanoparticles. Z.P. et al reported that Ni possesses a uniform and stable catalytic activity and carbon segregation across the surface of the catalyst, leading to improved CNT alignment [31].
The process of Ni deposition as a thin film can be carried out through various PVD methods such as sputtering, electron beam evaporation, thermal evaporation, dip-coating, drop-coating, and electrochemical plating. It is pertinent to mention that each deposition method has its own advantages and disadvantages, and a choice can be made based on the desired outcome. Furthermore, the process of catalyst particle formation is heavily reliant on the average thickness of the deposited Ni film. A thinner film gives a low surface coverage on the substrate, however, it can give separate catalyst particles.

On the contrary, thicker films lead to a more complete and fuller surface coverage during the deposition process at the expense of much larger nickel particles. Similarly, substrate heating during the deposition process also causes the formation of larger particles [32].

[30] reported a comparative study on the effect of catalysts on CNTs synthesized by thermal CVD. 50nm thick metal films of Fe, Co, and Ni were deposited on p-type plane silicon substrates before performing the chemical vapor deposition. The results showed Ni catalyst leading in terms of CNT growth whereby the length of vertically aligned CNTs was reported to be 20, 17, and 10 μm for Ni, Co, and Fe catalysts respectively. The average diameter of the CNTs was measured to be 100, 110, and 130 nm for Ni, Co, and Fe respectively. These results indicate Ni to be a preferable catalyst choice when a smaller CNT diameter and higher CNT growth are desired.

2.4 The Importance of a Current Collector

A current collector is a component that connects a supercapacitor with an external circuit, as well as supports the substrate for loading the active electrode material. It is a key component of the supercapacitor and can therefore influence the capacity, charge-discharge rate, thermal property, and long-term stability of a supercapacitor. This key component in conjunction with active electrode materials constitutes roughly 20% of the total weight of a supercapacitor cell. Consequently, it can significantly affect the gravimetric/volumetric specific energy density, power density, and lifespan of the supercapacitor. An ideal current collector should possess high electrical conductivity, low contact resistance, high specific surface area, stable bonding with the active electrode material, light weight, high mechanical strength, high electrochemical and thermal stability, and better prospects of mass production at lower costs. The key players in the supercapacitor market today namely AVX Corporation, SPEL Technologies Pvt. Ltd., Evans Capacitor Company, Tesla, etc. utilize carbon electrodes with organic electrolytes and aluminum current collectors in their supercapacitors. Research into the long-term cycle stability of these supercapacitors has revealed that the carbon layer tends to peel off from the smooth metallic current collector after certain charge-discharge cycles. This can significantly reduce the electrochemical performance. Recently, manufacturers have begun to use etched aluminum foils as current collectors instead of smooth foils. This has

led to the strengthening of the bond between the active electrode material and the current collector, and the prevention of the peel off. As a result, the supercapacitor now exhibits significantly improved electrochemical performance and stable operation even over tens of thousands of charge-discharge cycles [33], [34].

The importance of surface area since, a supercapacitor stores charges as a result of electrostatic double-layer capacitance (EDLC), which is a surface interaction, starkly contrasting with a conventional electrolytic capacitor that accumulates charge electrostatically, therefore, it can be deduced that an increase in specific surface area can increase charge accumulation [35]. To achieve a higher specific surface area, a microstructured current collector can be used which will allow more number of locations for charge adherence. An aluminum foil is used as a current collector for depositing the nanoparticle catalysts to grow carbon nanotubes afterward. The substrate foil is microstructured or pre-etched with the intention to increase the surface area. In comparison with a planar surface such as Si, the microstructured Al foil offers a higher surface area to accommodate more number of Ni nanoparticles as catalysts and consequently a higher CNT density. The choice of the substrate is largely dependent on the production of a high energy density supercapacitor. The intention is to use a substrate that possesses among other properties, excellent conductivity to facilitate ESR reduction in supercapacitors, reasonable chemical stability in organic electrolytes, and relatively inexpensive mass production. Aluminum possesses all of these qualities and many more – among them the most notable ones include, (i) superior conductivity in contrast with silver, gold, and copper for ESR reduction, (ii) Light weight with a low density to help improve the energy density ($\frac{Wh}{Kg}$) and power density ($\frac{W}{Kg}$) of supercapacitors, (iii) fabrication compatibility with irregular structures on the surface by a physical or chemical etching method, (iv) reasonable chemical stability in organic electrolytes used in supercapacitors, (v) high ductility to allow packaging of the supercapacitor structure into cylindrical, stacking or flat jellyroll cells, (vi) abundance of Al facilitates inexpensive mass production of the supercapacitors. [36]

2.5 Chemical Vapor Deposition (CVD) for CNT Growth

As discussed in section 2.2 about the role and advantages of carbon nanotubes for increasing the energy density and capacitance of supercapacitors, this section deals with their synthesis process. The chemical vapor deposition (CVD) technique is among the most commonly used methods for CNTs synthesis besides laser ablation and arc discharge methods. [11] This particular interest in the CVD method is fueled by its low cost and the ability to control carbon nanotube production, which can lead to better prospects of upscaling the entire process. This technique when using a catalyst is referred to as catalyst-assisted chemical vapor deposition. The process involves catalyst-assisted decomposition of hydrocarbons (typically acetylene or ethylene), in a tube furnace/reactor at high temperatures in the range of 550-750˚C, followed by the growth of CNTs over the catalyst. As per the literature, the best results have been obtained with Ni, Fe, or Co nanoparticles as catalysts [37]–[39]. The carbon precipitates from the saturated catalyst particle and forms tubular carbon structures that are typically called nanotubes [40]. The CVD process typically involves three key steps for CNT synthesis i.e. (i) – the precursor decomposes on the catalyst and the catalyst-C bond forms, (ii) – carbon diffuses through the catalyst towards CNT synthesis, (iii) – the precursor molecule experiences gas-phase reactions which can influence the overall CNT growth [27]. The nanotubes grow out of the catalyst nanoparticle by either tip growth or base growth, the two mechanisms largely governed by the contact force or interaction strength between the catalyst and the substrate. Since these nanotubes are growing directly out of the nanoparticle so their diameter is also directly dependent on the catalyst nanoparticle size. It is also pertinent to mention here that the literature suggests that the dimensions of the nanoparticle as well as the resulting nanotube are also influenced by several other parameters such as film thickness, temperature, and the composition of the catalyst etc. Stronger interactions lead to base growth as the particle is prevented from leaving the surface of the substrate, which causes the catalyst particle to get stuck at the base of the formed nanotube. On the other hand, a weak interaction causes tip growth because the formation of CNT pushes the catalyst particle toward the tip of the nanotube [41]. The base growth is known to exhibit certain limitations contributed by gas phase species diffusing through long and dense CNTs [42]. However, these limitations are absent in tip growth as the catalyst remains at the tip of the nanotube and is exposed to the gas phase

of the furnace. Literature also suggests that plasma-enhanced low-pressure CVD results in nanotubes which are highly curved, tangled and randomly oriented, while for the atmospheric pressure thermal CVD (APCVD), the CNTs possess a regular distribution with straighter orientation. Furthermore, it is reported that longer and straighter carbon nanotubes featuring diameters as small as 10 nm can be synthesized using thin Ni layers. [32]

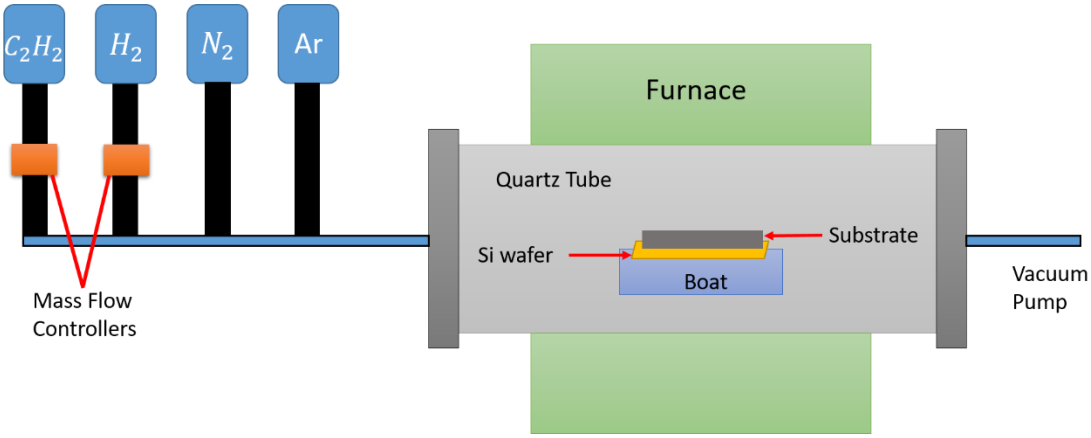

Figure 5: CVD Apparatus

2.6 Sputtering

Sputtering is a physical vapor deposition (PVD) technique used for producing films and coatings. PVD is a process in which a desired material can be made to change from a condensed phase to a gas phase and then back to the condensed phase of the film [43]. Sputtering is the phenomenon of bombarding positively charged ions on negatively charged target material to achieve the ejection of atoms from the surface. It is achieved through the collisions between the incident energized particles, and the resultant recoil atoms, with surface atoms. These sputtered target atoms are knocked out with substantial kinetic energies, which can significantly alter the kinetics of the film growth, the particle/cluster size, as well as the microstructure. The sputtering technique is preferred in cases when a low-temperature process is desired, however, a drawback of this PVD technique is a slow deposition rate. In order to improve the deposition rate, a different technique is used which is called the “DC magnetron” or “RF magnetron”

sputtering. Both of these sputtering techniques involve the use of a magnetic field in the system. The RF magnetron sputtering is typically used for non-conductive target materials whereas the DC magnetron sputtering is utilized for conductive target materials. The deposition rate during the sputtering process can be significantly improved using either of the techniques.

2.7 DC Magnetron Sputtering

The DC magnetron sputtering involves the generation of plasma using DC power. A working gas such as argon (Ar) is introduced into the chamber which provides for a medium to initiate and sustain the electrical discharge. A glow discharge plasma is required for the generation of ions which are then attracted towards the negatively charged target. Plasma is the fourth state of matter and can be described as a partially ionized gas. The ionization of a sufficient number of gas atoms leads to the generation of plasma. Plasmas are governed by the density of charged species which forms the basis of their categorization. The so-called glow discharge plasma that is a part of the sputter deposition process lies in the middle range having ion densities between 10^8 and 10^4 per cm^3 [44]. A typical way to generate plasma for the sputtering process is to use two metal electrodes – a cathode and an anode – enclosed in a vacuum chamber. The chamber is first evacuated and then a few hundred volts are applied to the cathode resulting in a visible glow between the cathode and the anode. The plasma ignition can be thought of as analogous to the dielectric breakdown in an insulating solid as in this case also the originally insulating gas begins to conduct at a critical voltage. When a voltage is applied between the electrodes, an electric field is created which accelerates the free electrons on the cathode towards the anode. The electron attains energy and collides with a neutral gas atom, thereby ionizing it. The following reaction takes place where the two resulting electrons bombard two other neutrals while the argon ion is accelerated for collision with the cathode target, releasing secondary electrons. This leads to a snowball effect which is sustainable for maintaining plasma from the so-called glow discharge [45].

$$e^- + Ar \rightarrow 2e^- + Ar^+$$

Magnetron sputtering is known for certain advantages over other deposition techniques such as high deposition rates [46], high-purity films, high adhesion of films, excellent

uniformity on large area substrates, as well as the ease of sputtering any metal or compound [47]. One disadvantage of the sputter deposition process is non-conformal deposition, which means that it is not optimized for non-planar surfaces, such as porous ones. This prevents the nanoparticles to reach all the way down into the depths of the pores, and causes a shadowing effect as depicted in Figure 6.

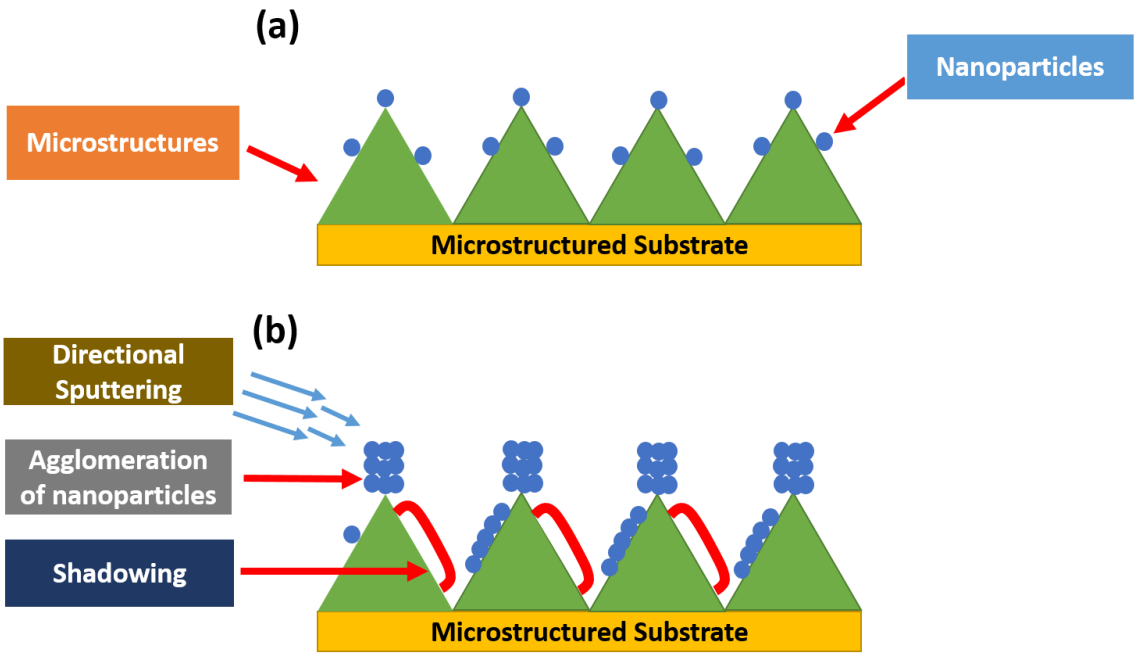

*Figure 6: **(a)** shows the first few nanoparticles sputtered on a microstructured substrate, **(b)** shows non-conformal deposition causing shadowing after a few minutes.*

2.8 Important Parameters

This section deals with certain key parameters involved in the DC magnetron sputtering process. The parameters are set based on the desired outcome of the thin film deposition. The controllable parameters include the base pressure, working pressure, applied power (*for sputtering rate*), and substrate temperature. The effect of most of the parameters is well defined, however, some of them are tightly intertwined–meaning changing one can affect the other. A brief description of each parameter and its effect is presented.

Base pressure is maintained inside the vacuum chamber before the sputter deposition process is initiated. This parameter reduces contaminants from inside the chamber, resulting in a thin film with marginal contamination. Typically oxygen contributes the most to the contamination and it is not possible to completely avoid its effect. There is always the possibility of oxygen being trapped inside the thin film during the deposition process. The base pressure prevalent in the literature is in the order of 10^{-6} to 10^{-9} Torr [48]. In general, low base pressure provides better results.

The following equation shows the relation of film deposition rate with key sputtering parameters [49]:

$$R = \frac{k\ .\ P}{\rho\ .\ d} \dots\dots\dots\dots\dots\dots\dots\dots\dots\dots\dots\dots\dots\dots\dots \textit{2.1}$$

In this equation, k is constant of proportionality, ρ is gas pressure, P is the power, and d stands for electrode distance. As it can be seen that power has a direct relationship with the deposition rate R, therefore film deposition rate undergoes a linear change with the power. This is owing to the fact that increasing the power raises the kinetic energy of the Ar atoms that strike the target material causing it to sputter. This high kinetic energy is then transferred to these ejected atoms that travel at a faster pace toward the substrate for coating. Another effect of increasing the applied power is that the substrate temperature rises because of heavy bombardment of the approaching sputtered atoms. This in turn increases the mobility of adatoms and causes coalescence which results in larger grain sizes or clusters. Gas pressure and electrode distance on the other hand are inversely related to the deposition rate, so any increase in these will cause the deposition rate to decline.

The working/gas pressure (P) is dictated by the amount of gas flow (Ar) inside the vacuum chamber. It is related to the energy of adatoms and this relationship is based on the kinetic theory which suggests that the mean free path of the gas molecules has an inverse relationship with the gas pressure. If the gas flow is increased, it will reduce the mean free path (MFP), which in turns leads to a reduction in the deposition rate [50]. The MFP decides the longest distance a sputtered atom can travel towards the substrate before colliding with an argon gas atom. The collisions can reduce the kinetic energy of the

sputtered atom causing the atom to not reach the substrate at all either due to loss of energy or scattering on the walls [51]. The working pressure is also known to influence the grain size of the deposited material on the substrate.

Even without substrate heating switched on, the continuous bombardment of the energetic particles onto the substrate can cause self-heating of the substrate and contribute to agglomeration of nanoparticles [52].

3 Research Methods and Experimental Procedures

3.1 Sample Preparation for Thin Film Deposition

The pre-etched/microstructured aluminum foil was used for depositing thin Ni layers of varying thickness levels and at different powers (*sputtering rates*). A total of 9 samples were chosen for experimentation as presented in Table 1. Samples measuring 18 x 12.5 cm were first degreased with acetone (C_3H_6O) and then immersed in isopropanol (C_3H_8O) for 10 minutes. The samples were then retrieved and washed with distilled water and then blow-dried with high pressure nitrogen. To further remove the moisture, the samples were heated on a hot plate for 2 minutes on each side at 100˚C.

Table 1: Represents the 9 different samples chosen for experimentation and analysis.

Thickness (nm)	Powers (W)
10	25, 100, 400
100	25, 100, 400
250	25, 100, 400

3.2 Sputter Deposition

3.2.1 Modification of Magnetron for Mounting Nickel Target

A nickel target 99.9% pure with dimensions 3.00”D x 0.250”T was loaded inside the AJA International Sputter machine model ATC 20x20x30. The current configuration features 3 sputter guns as presented in Figure 9. The development of rings on the Ni target

material is caused by the line of force of magnetic field over time. A modification of the magnetron magnets was made whereby the central magnet was taken out because nickel is a ferromagnetic material. The central magnet in a magnetron sputtering system is responsible for generating a magnetic field that traps electrons near the target surface, thereby enhancing the ionization rate of the sputter gas and improving the overall efficiency of the sputtering process. Since the material being used is ferromagnetic, which means it is strongly attracted to magnetic fields. If the magnetic field near the target surface gets too strong, it can cause the magnetization of the Ni target and decrease the efficiency of the sputtering process. Therefore, the central magnet is removed to reduce the magnetic field near the Ni target to prevent magnetization and enhance the quality of the sputtered film. As a drawback, the sputtering rate was slightly reduced as the absence of the magnetic field led to a lower ionization rate of the sputter gas. Furthermore, the distance between the target and the substrate was optimized to be 18 cm for improving the thin film uniformity.

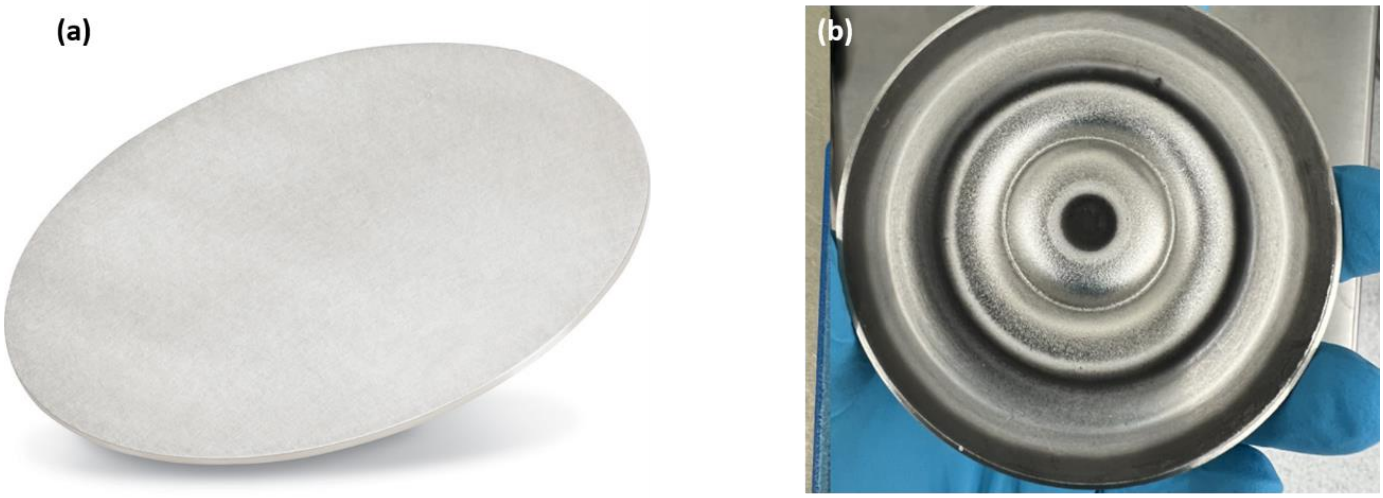

Figure 7: ***(a)*** *Newly purchased smooth Ni target,* ***(b)*** *development of rings can be observed after use.*

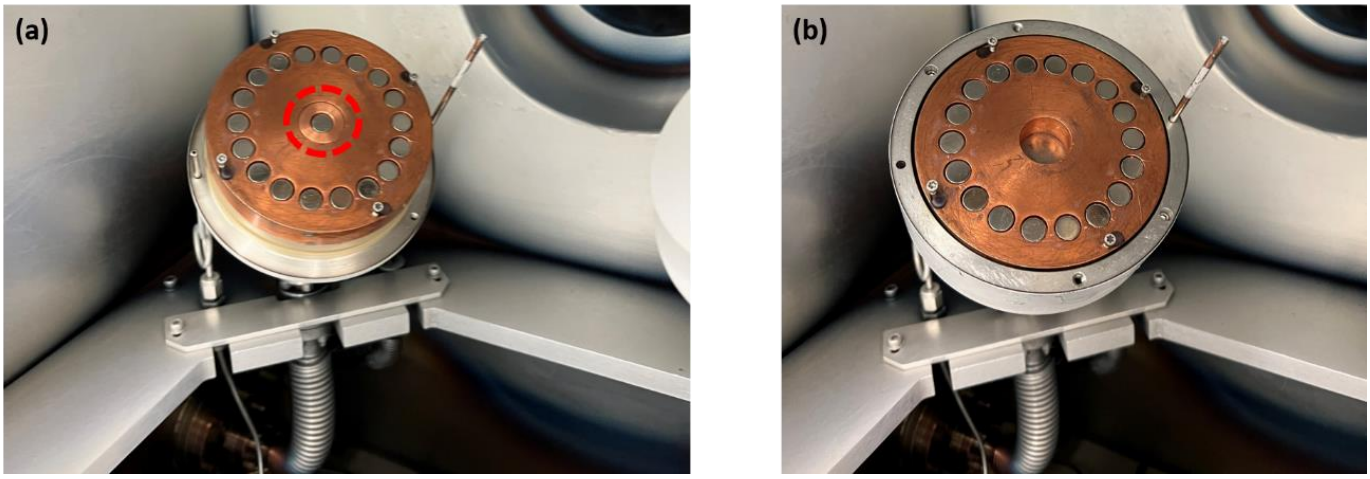

Figure 8: ***(a)*** *magnetron system with the central magnet in place,* ***(b)*** *modified magnetron system with the central magnet removed for compatibility with the Ni target.*

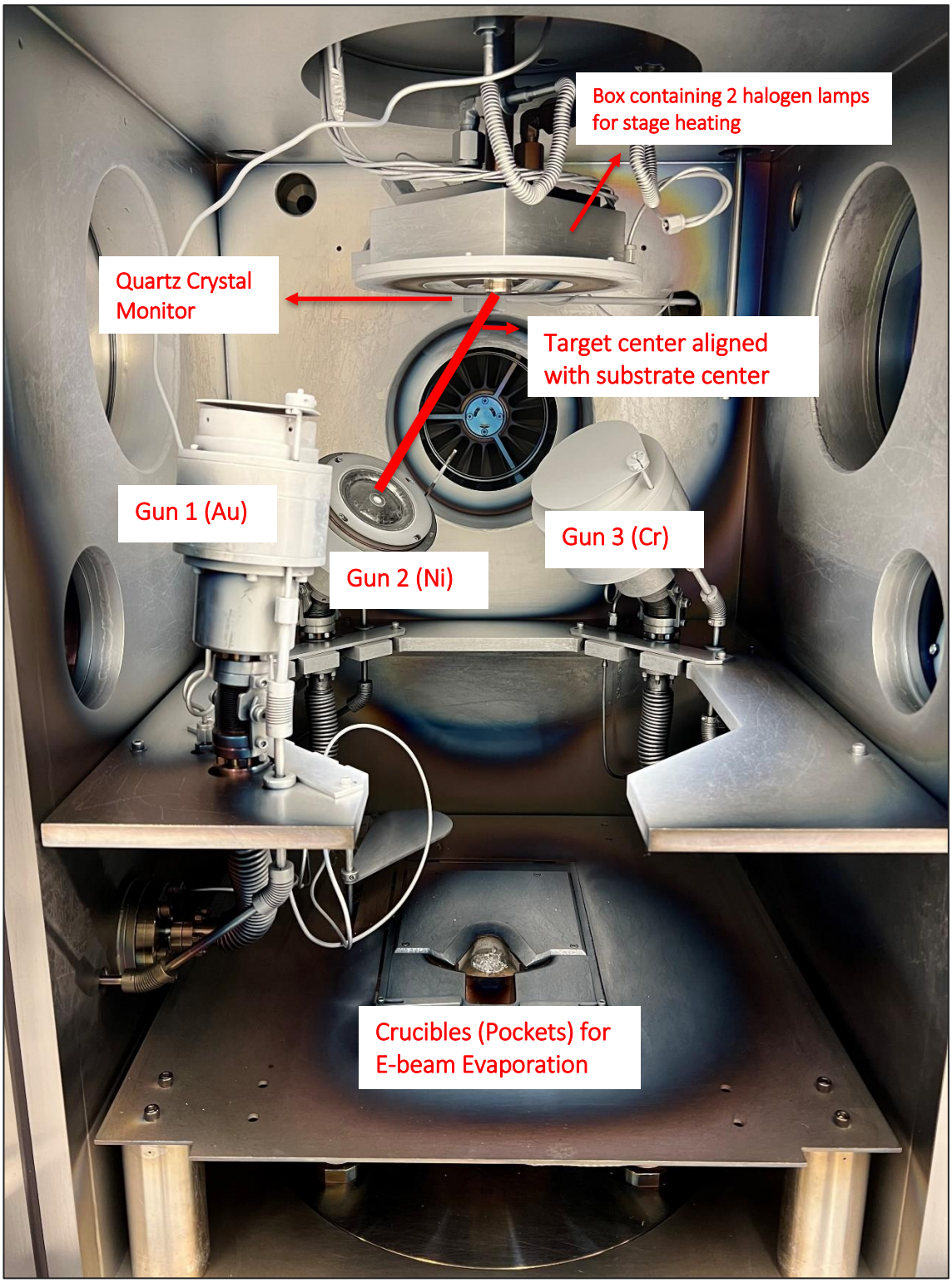

Figure 9: Illustration of magnetron sputtering setup from inside the chamber.

3.2.2 Nickel Deposition Process

The cleaned samples were then loaded on the sample holder provided with the AJA International Sputter machine model ATC 20x20x30. Certain deposition parameters including argon flow of 15 sccm and applied power were input into the software program that is loaded on the computer attached to the sputtering machine. A shutter arrangement was provided for pre-sputtering for 15 minutes at 100 W applied power to reduce the effect of contamination caused by other metals inside the chamber by other users of the Sputter AJA. Next, the rotation of the sample holder was set to 10 turns/min for uniform coating. Since additional thermal energy can increase the ad-atom mobility and diffusion leading to increased particle size, therefore the substrate heating was left switched off as the motive was to keep the particle size as small as possible for enabling the growth of thinner diameter CNTs later on. The applied power was set to 25W and the sputter deposition was started until the film thickness of 10nm Ni was reached. Similarly, deposition of 10nm was performed at 100W and 400W. Next, films of 100nm and 250nm were deposited at the same set of power levels i.e. 25W, 100W and 400W. The sputter AJA equipment uses a Quartz Crystal Monitor (QCM) to monitor the amount of thin film deposited on the Al substrate. The QCM follows the piezoelectric effect and has a Q factor as high as 10^6 and resolution down to 10 Hz. Its working principle is such that it measures a mass variation per unit area by calculating the change in the frequency of a quartz crystal resonator. The oscillation frequency of the crystal decreases as the crystal's mass increases due to the Ni material being deposited on it. The QCM relies on the density of the material and the Z-factor responsible for matching the acoustic properties of the material being deposited to the acoustic properties of the base quartz material of the sensor crystal.

$$Z - factor = \frac{Z_q}{Z_m} \quad \text{..... 3.1}$$

Z_q and Z_m represent acoustic impedances of quartz and material respectively.

The applied powers with corresponding deposition rates are presented in the Table 2. After the deposition of thin films, the microstructured samples were retrieved for characterization to study the morphology, size and distribution of the nanoparticles and clusters.

Table 2: Applied sputter powers and their corresponding deposition rates in Å/s.

Power (W)	Deposition Rate (Å/s)
25	0.14
100	0.77
400	3.2

Table 3: Important parameters used for the sputtering process.

Base Pressure	$3.6\ x\ 10^{-5}\ Torr$
Working Pressure	$1.08\ x\ 10^{-2}\ Torr$
Substrate to target distance	$18\ cm$
Substrate temperature	$Room\ temperature\ (20°C)$
Argon flow	$15\ sccm$
Stage Rotation	$10\ turns/min$

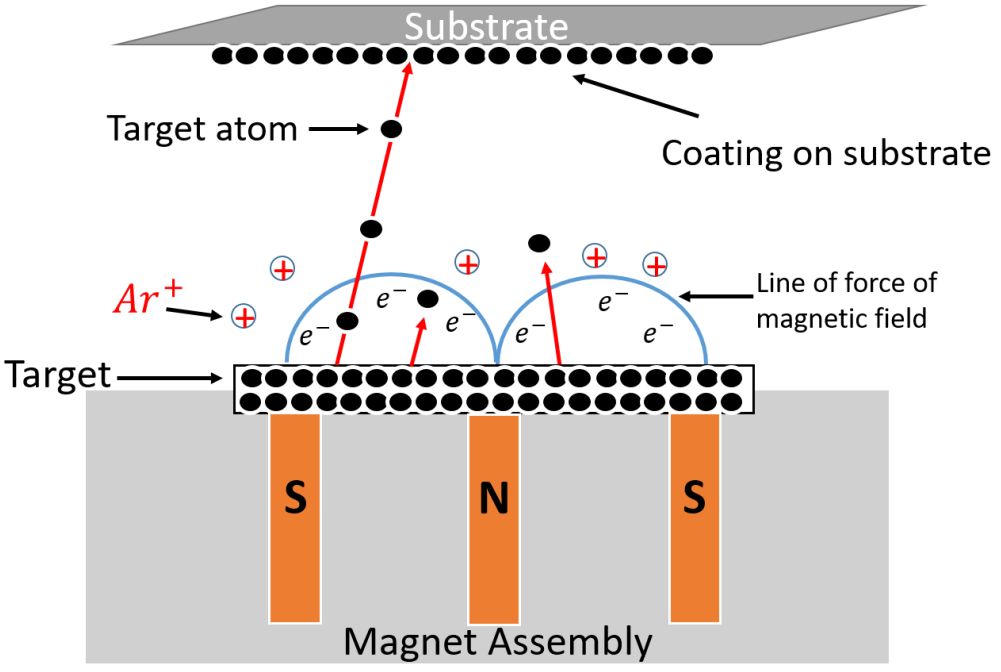

Figure 10: Schematic of Magnetron Sputtering Process.

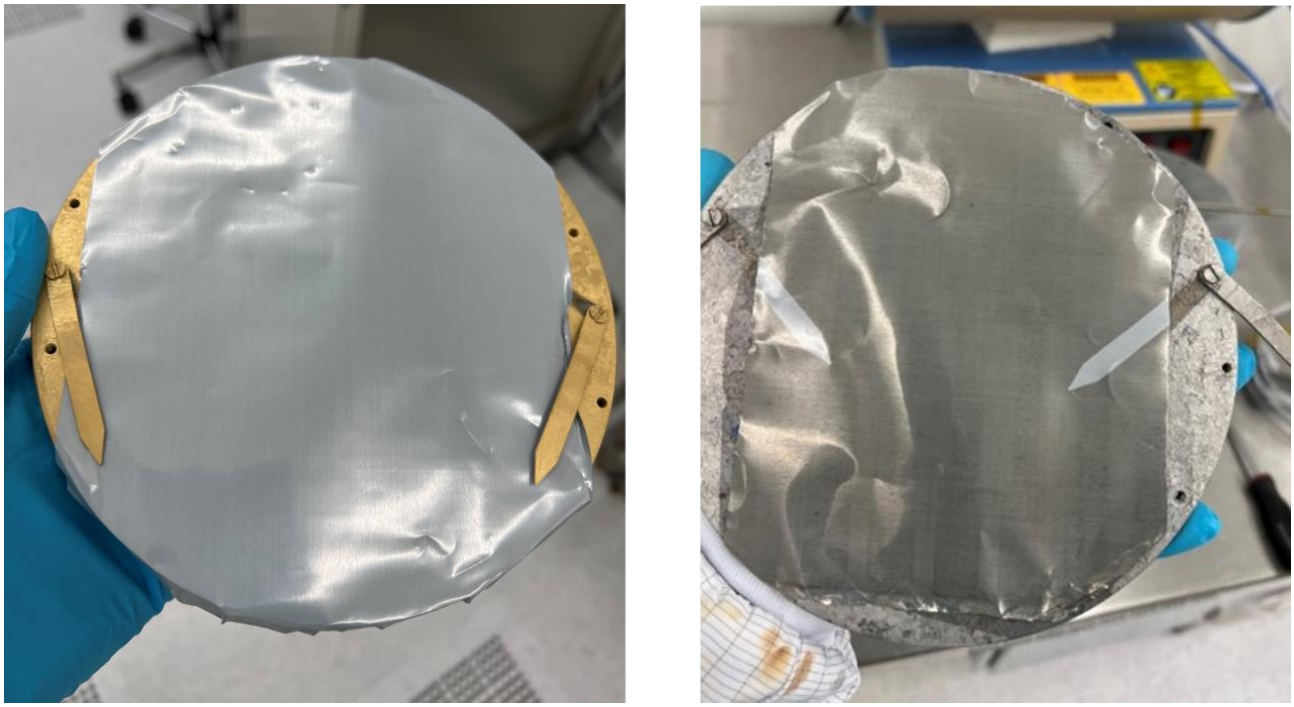

Figure 11: The Al foil mounted on the sputtering stage, before (left) and after (right) Ni sputtering.

3.3 Characterization Using Scanning Electron Microscope

A Scanning Electron Microscope (SEM) is a characterization tool that generates a range of signals at the surface of solid specimens by utilizing a focused beam of high energy electrons at the object. It offers far superior resolution than an optical microscope due to shorter electrons wavelength. Hitachi SU 3500 (Figure 12) was utilized for characterization of the carbon nanotubes (CNTs) as it offers the flexibility to go up to 300kX magnification. Using this equipment, important information such as the morphology, chemical composition, material orientation, and crystalline structure can be obtained from the electron-sample interactions. Typically, a specific area of the surface of the object under observation is selected and a two-dimensional image for data collection, and a two-dimensional image is produced that shows spatial variations [53]. The depth of the sample surface until which the signals are desired to be sent can be adjusted by changing the accelerating voltage V_{acc}. Accelerating voltage between 5 and 15 kV was used during characterization. Normally, secondary electrons (SE) mode is deployed for imaging – these are the outer shell electrons. This equipment was utilized

for characterizing the carbon nanotubes – both for CNT carpet height and CNT diameter measurements.

A Field Emission Scanning Electron Microscope (FESEM) was utilized for characterizing the thin films. The FESEM attains enhanced spatial resolution by utilizing a field emission cathode in the gun that leads to narrowing of the probing beams. The Hitachi SU 8230 offers magnification of 1000kX resulting in a much higher resolution image of the sample surface and was therefore utilized for studying the morphology, size and distribution of the Ni nanoparticles. Both the top view of the thin films and the cross-sectional view were characterized using FESEM.

Figure 12: Hitachi SU 3500 (left) and Hitachi SU 8230 (right).

In addition, Energy Dispersive X-Ray Spectroscopy (EDX) – a function of the FESEM – was utilized for elemental analysis and mapping of the as-deposited substrates. It can determine what elements are present in a given material as well as the amount of each element. Its working principle is such that a high energy electron beam is made to hit the sample so that the inner shell electrons of the sample atoms are knocked out. This creates a vacancy which is filled by an electron of higher energy. A photon or in the case of EDX, a characteristic X-ray carries the excess energy which is detected in the spectrum. The elemental mapping was also performed for obtaining the elements distribution across

the scanned area. The mapping shows the X-ray data for different energy ranges as separate elemental images. It was performed to observe the presence of the Ni layer and its extent of penetration inside the microstructured Al samples. The schematic (Figure 13) describes the basic working principle of EDX whereby an incident electron dislodges and knocks out a K-shell electron. Next, an electron from the L-shell fills this vacancy and excess energy is released as a characteristic x-ray. This is then detected and recorded in the spectrum.

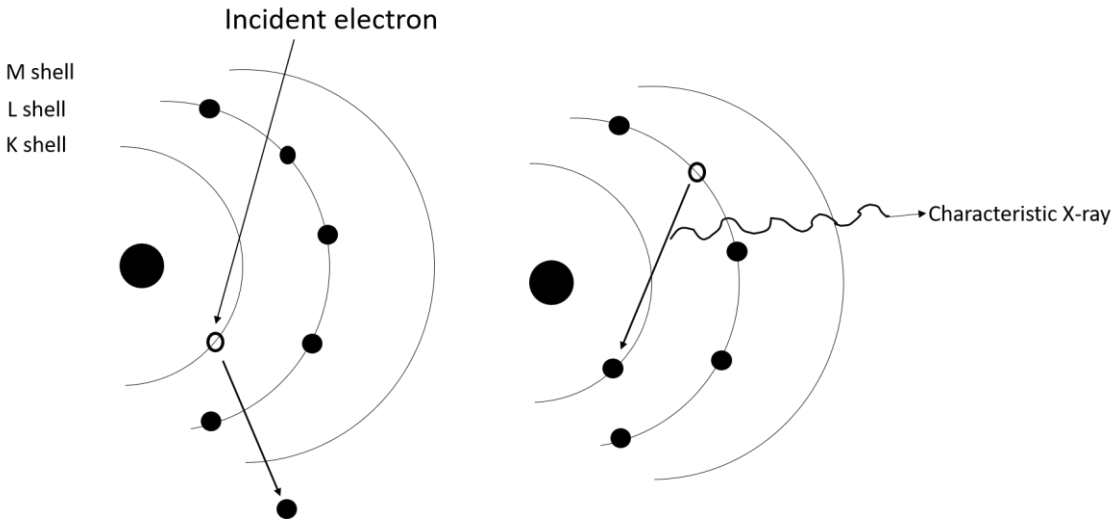

Figure 13: Working principle of EDX.

3.4 Nanoparticle Morphology and Distribution Analysis using ImageJ

ImageJ is an open source image processing software developed to analyze multidimensional images. It has several functions and plugins to perform the analysis. This software was utilized to study the morphology, size and distribution of the Ni nanoparticles and clusters on the Al surface. The image was first changed to 8-bit, then the scale bar was measured using the provided line tool and then the scale was set using the "set scale" tool. An area was selected from the image under observation using the "rectangle" tool and then further processing was performed on it. FFT bandpass filter was applied to the selected area of the image with values for "filter large structures down to" set to 20 pixels and "filter small structures" set to 3 pixels. This step was performed to

facilitate the measurement and analysis process as it can make the nanoparticles/clusters pop with clear boundaries around them. The bandpass filter entails the deletion of high spatial frequencies (i.e. blurs the image) and low spatial frequencies (i.e. subtracts a blurred image). Next, for smaller thin films i.e. 10 nm, the "threshold" function was used for the automatic selection of the nanoparticles and then the function "analyze particles" was used for measuring their area. The "circularity" value was chosen from 0.00-1.00 in order to accommodate all nanoparticle shapes. For films larger than >10 nm i.e. 100 nm and 250 nm, the "polygon selection" tool was used and the selections were made manually with the mouse cursor since the "threshold" function is only suitable for tiny individual nanoparticles.

3.5 Calculation of Spatial Density and Surface Coverage

The spatial density and surface coverage of Ni nanoparticles are two important parameters that can determine the density of CNTs after CVD. These were calculated using the following formulae:

$$Spatial\ Density = \frac{Number\ of\ nanoparticles}{Specified\ area\ under\ observation} \quad \text{.....3.2}$$

$$Surface\ Coverage = \frac{\Sigma A_{Ni}}{Specified\ area\ under\ observation}\ x\ 100 \quad \text{..... 3.3}$$

3.6 CNT Synthesis Using Atmospheric Pressure Chemical Vapor Deposition (APCVD)

Multi-walled iCL-CNTs were grown through atmospheric pressure chemical vapor deposition (APCVD) process. GSL1100X high temperature vacuum tube furnace was used with a tube size of 4.3ID x 4.90D x 61L cm. The samples were reduced to dimensions of 1.5 x 1 cm for fitting them in the glass boat. The samples were placed on a silicon wafer to provide for height so the as-deposited substrate is adequately exposed to the reacting gases inside the reactor tube for optimal CNT synthesis. A "water bubbler" arrangement

was also provided as H_2O is considered to prolong the catalyst lifetime by etching carbon byproducts that cover and deactivate the catalyst particles and by blocking the Ostwald ripening of the catalyst. A temperature of $600^{\circ}C$ was chosen which is well below the melting point of Al ($660^{\circ}C$), and acetylene (C_2H_2) was chosen as a highly reactive carbon feedstock as it is a known and effective direct growth precursor. The CVD furnace was initially at room temperature i.e. $20^{\circ}C$ and was programmed in such a way that it reached the desired temperature of $600^{\circ}C$ in 58 minutes. The APCVD was performed in the argon environment flown inside the tube at $40\ sccm$, and when the temperature of $600^{\circ}C$ was reached, H_2 gas at $100\ sccm$ and C_2H_2 at $20\ sccm$ were flown during the $60\ minutes$ CNT synthesis period. Next, N_2 at $200\ sccm$ was used to cool down the tube and the samples containing CNTs were retrieved for characterization and mass loading measurement.

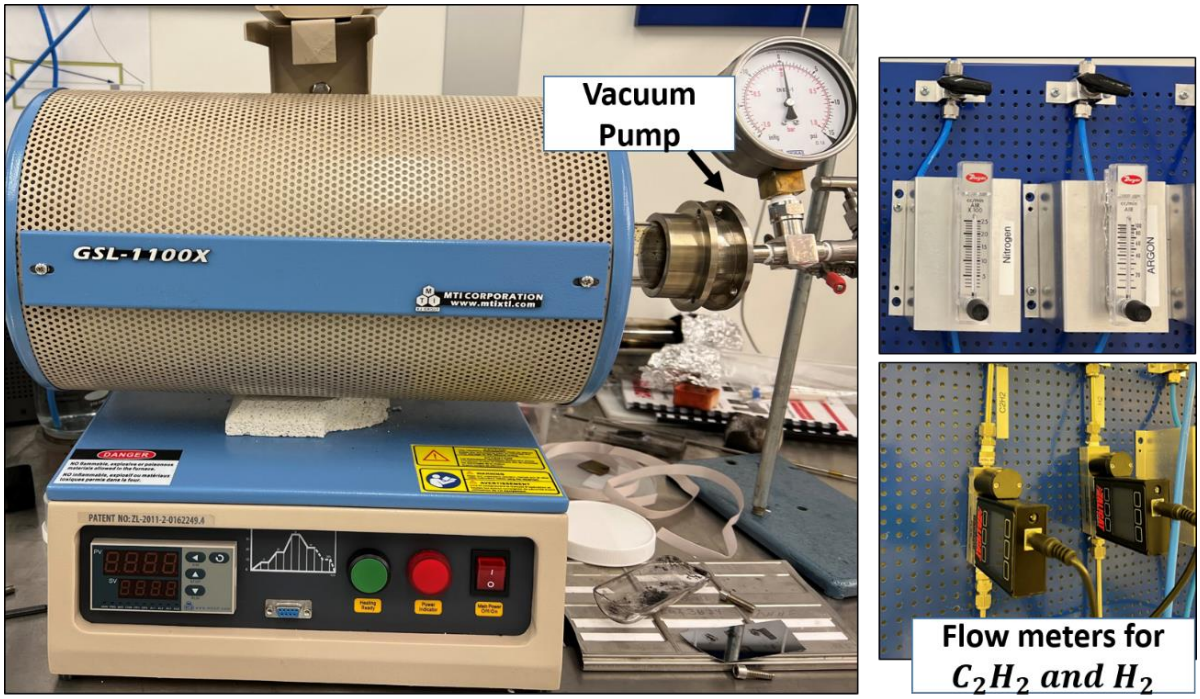

Figure 14: CVD furnace used for CNT synthesis.

3.7 Calculation of CNT Mass Loading

Mass loading of carbon nanotubes refers to the measure of the quantity of CNTs within a given mass or volume. It is a crucial parameter in determining the capacitance of a

supercapacitor as it can influence the available surface area for charge storage in SC. A higher mass loading is indicative of an increased electrode surface area, and thus improved electrochemical activity and capacitance. This is because having an increased surface area paves the way for a higher number of electrochemical reactions to take place at the electrode-electrolyte interface. This then leads to higher charge storage. The CNT mass loading was calculated using the following formula:

$$CNT\ Mass\ Loading\ \left(\frac{mg}{cm^2}\right) = \frac{CNT\ mass(mg) - Ni\ thin\ film\ mass(mg)}{Total\ area\ of\ specimen\ (cm^2)} \quad \text{.....3.4}$$

4 Results & Discussion

4.1 Morphology and Distribution of Ni Nanoparticles – Top View

High resolution images of the microstructured Al foil of 70µm thickness, both from the top and cross-section are presented to establish grounds for comparison before and after Ni deposition.

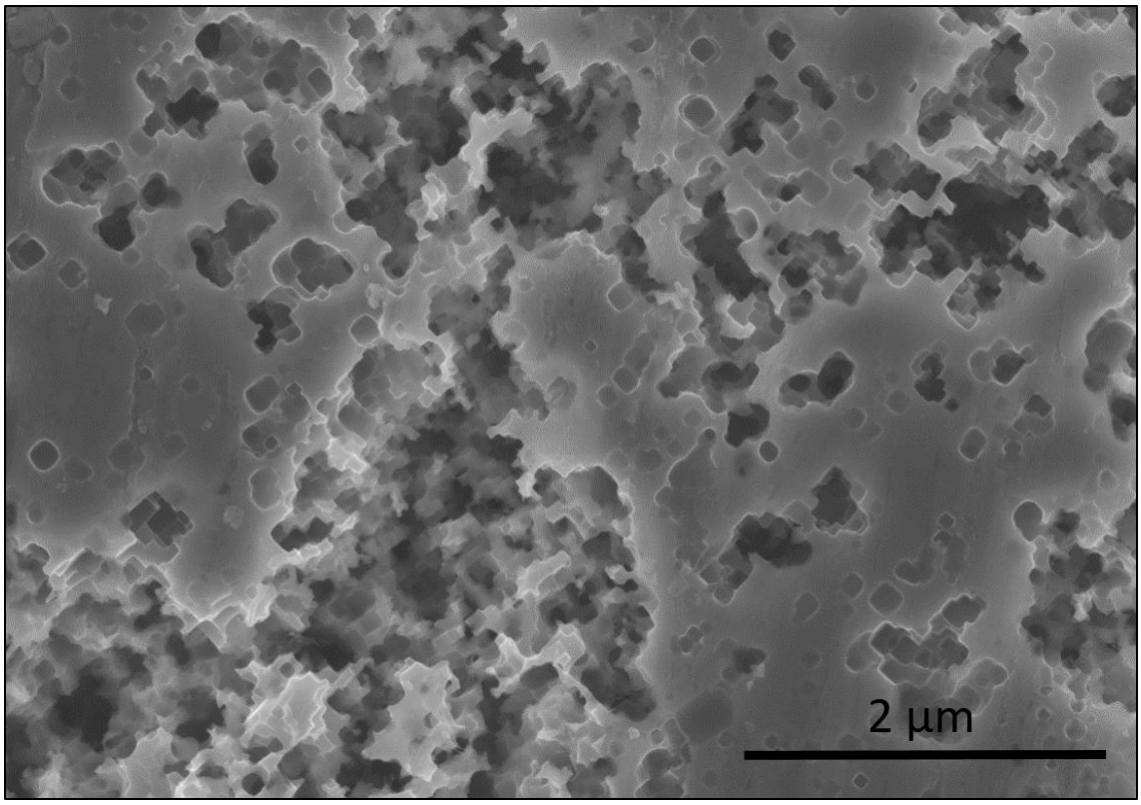

Figure 15: Top view of microstructured Al foil substrate.

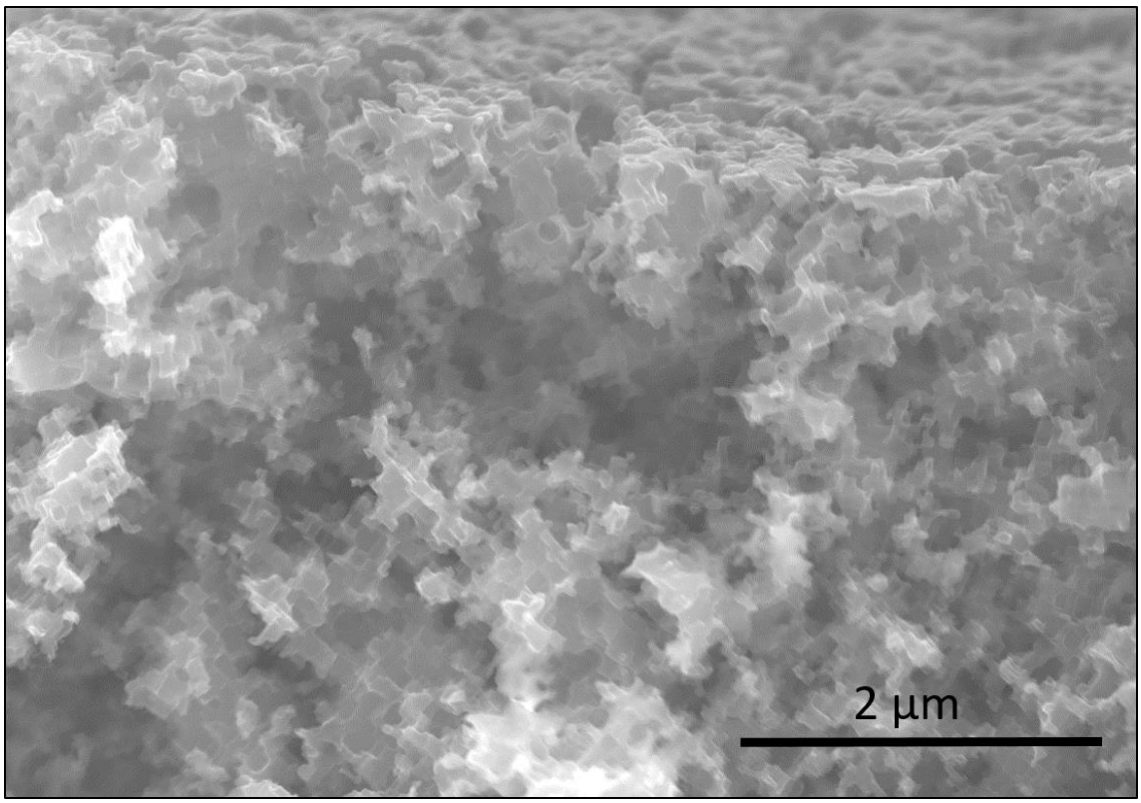

Figure 16: Cross-sectional view of microstructured Al foil substrate.

Before presenting characterization, morphology and distribution results of Ni thin films on the microstructured substrate, it is pertinent to mention that the sputtering equipment is optimized for planar surfaces such as silicon wafers. The substrate used for experimentation, however, is microstructured, and thus non-planar. A thin film of certain thickness, for example, 100 nm, sputtered onto a microstructured substrate is measured to exhibit a different (*usually larger*) film thickness due to larger surface area contributed by porosity of the substrate. Fig. 18 presents what 100 nm thin film appears on a planar Si substrate. The film appears to follow columnar growth. During the sputtering process, initially the ejected target atoms form nuclei on the substrate. The nuclei then grows into larger nanoparticles as the deposition process continues. The distance between neighboring particles decreases and adjacent nanoparticles come into contact and join with each other, creating larger particles [54]. It can also be argued that the larger nanoparticles are a result of surface diffusion, whereby atoms on the surface of the nanoparticles partake migration to the particle's interior, resulting in particle growth.

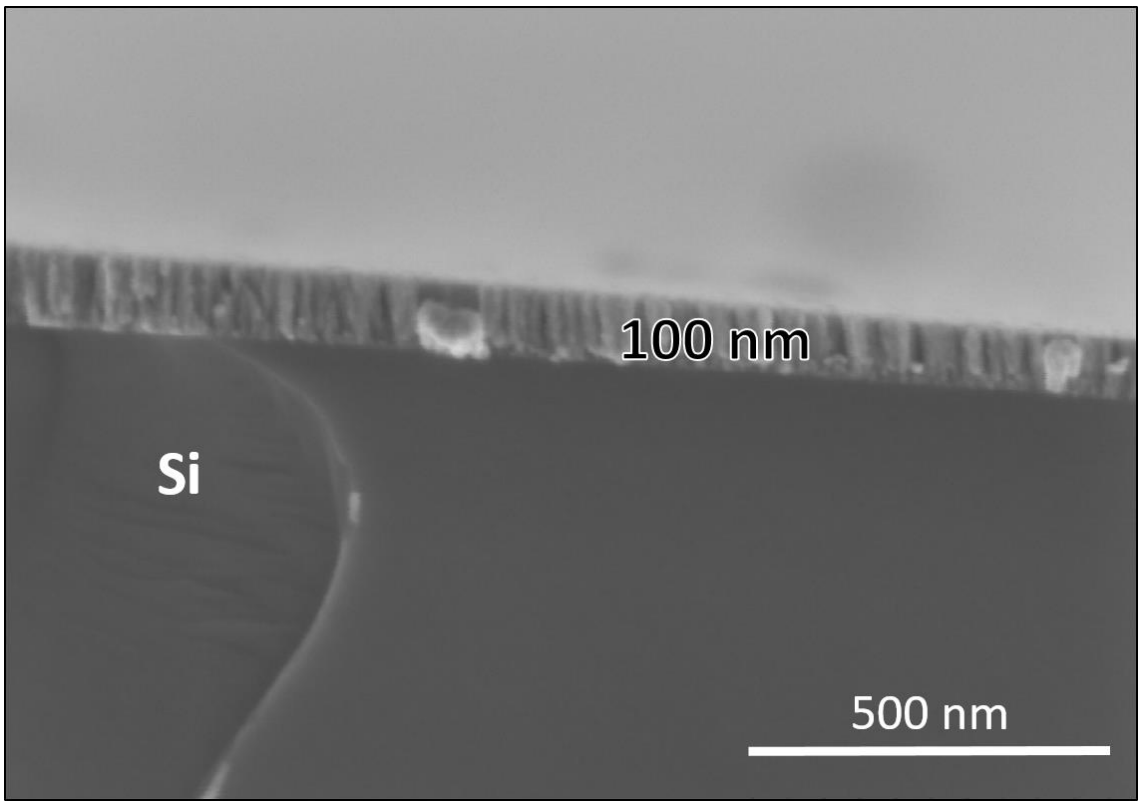

Figure 17: Planar Si substrate with 100 nm sputtered Ni thin film.

Morphology and size distribution of Ni nanoparticles as a 10 nm thin film on the microstructured Al foil is performed (Fig. 19). Small size nanoparticles are observed scattered all over the substrate. The low density of nanoparticles is caused by very small film thickness, and the appearance of a porous structure throughout the substrate is due to inadequate coverage of the Ni nanoparticles.

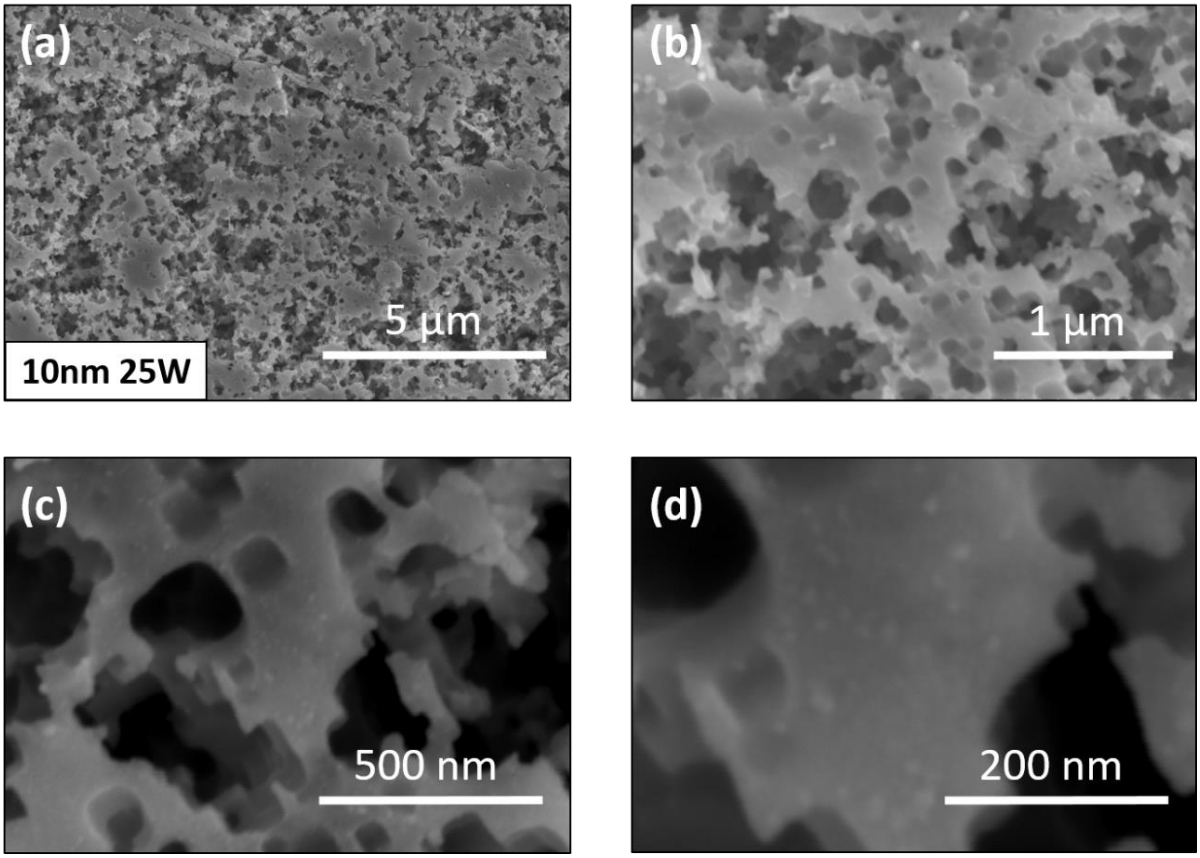

*Figure 18: FESEM images - **(a)**, **(b)**, **(c)**, and **(d)** represent the Al foil with 10 nm @ 25W (0.14Å/s) as-deposited Ni thin film.*

An area measuring $34933.830\ nm^2$ was selected (*presented as dashed rectangle in red in Fig 19a*) for calculating the Ni nanoparticle diameter, distribution, spatial density, and surface coverage. A FFT bandpass filter was applied on the selected area for creating a contrast and enhancing the appearance of nanoparticles with clearly defined boundaries. Next, the threshold function was used to highlight and make a selection of the nanoparticles. For 10 nm thin film sputtered @ 0.14 Å/s (25 W) the diameter of 71 differently sized Ni nanoparticles was considered and the mean diameter was calculated to be $7.76\ nm$.

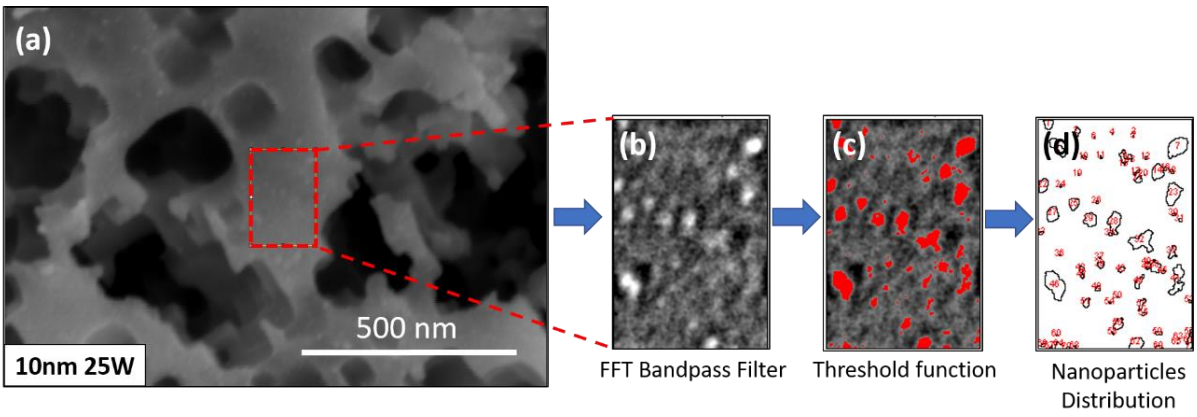

Figure 19: ***(a)*** *selected area for processing,* ***(b)*** *FFT bandpass filter for enhancing contrast,* ***(c)*** *threshold to highlight and select nanoparticles,* ***(d)*** *distribution of nanoparticles.*

For 10 nm thin film sputtered @ 0.77 Å/s (100 W), the diameter of 128 differently sized Ni nanoparticles was considered and the mean diameter was calculated to be $8.01\ nm$.

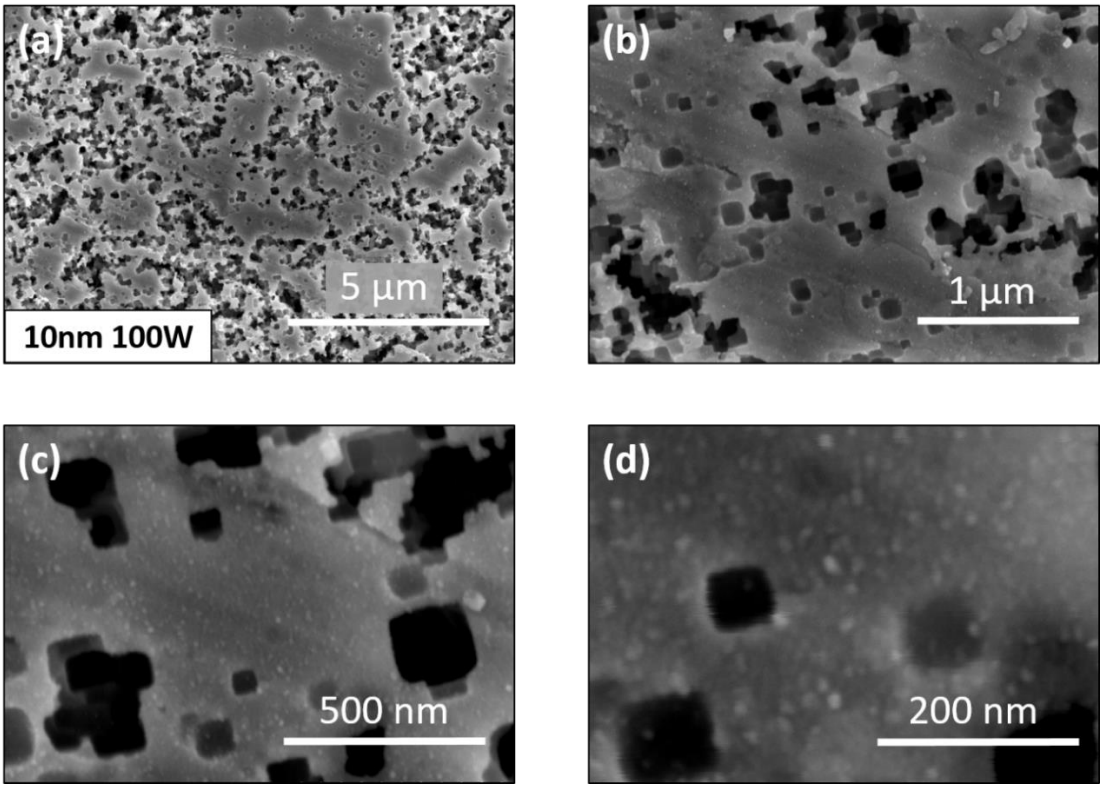

Figure 20: FESEM images - ***(a)****,* ***(b)****,* ***(c)****, and* ***(d)*** *represent the Al foil with 10 nm @ 100W (0.77Å/s) as-deposited Ni thin film.*

An area measuring $64906.344\ nm^2$ was selected from the as-deposited Al foil surface (*presented as dashed rectangle in red in Fig 21a*) for measurement of the Ni nanoparticles size, distribution, and spatial coverage among other parameters.

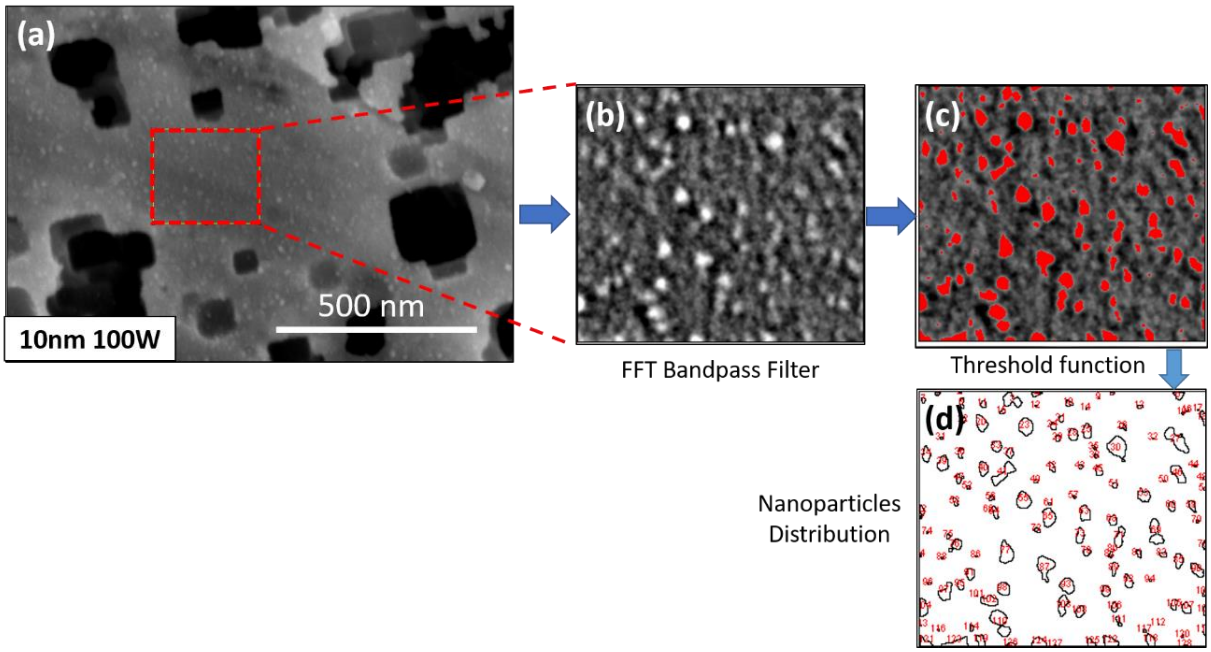

Figure 21: ***(a)*** *area selection,* ***(b)*** *FFT bandpass filter,* ***(c)*** *threshold function,* ***(d)*** *nanoparticles distribution.*

For 10 nm thin film sputtered @ 3.2 Å/s (400 W), the diameter of 57 differently sized Ni nanoparticles was considered and the mean diameter was calculated to be $8.95\ nm$.

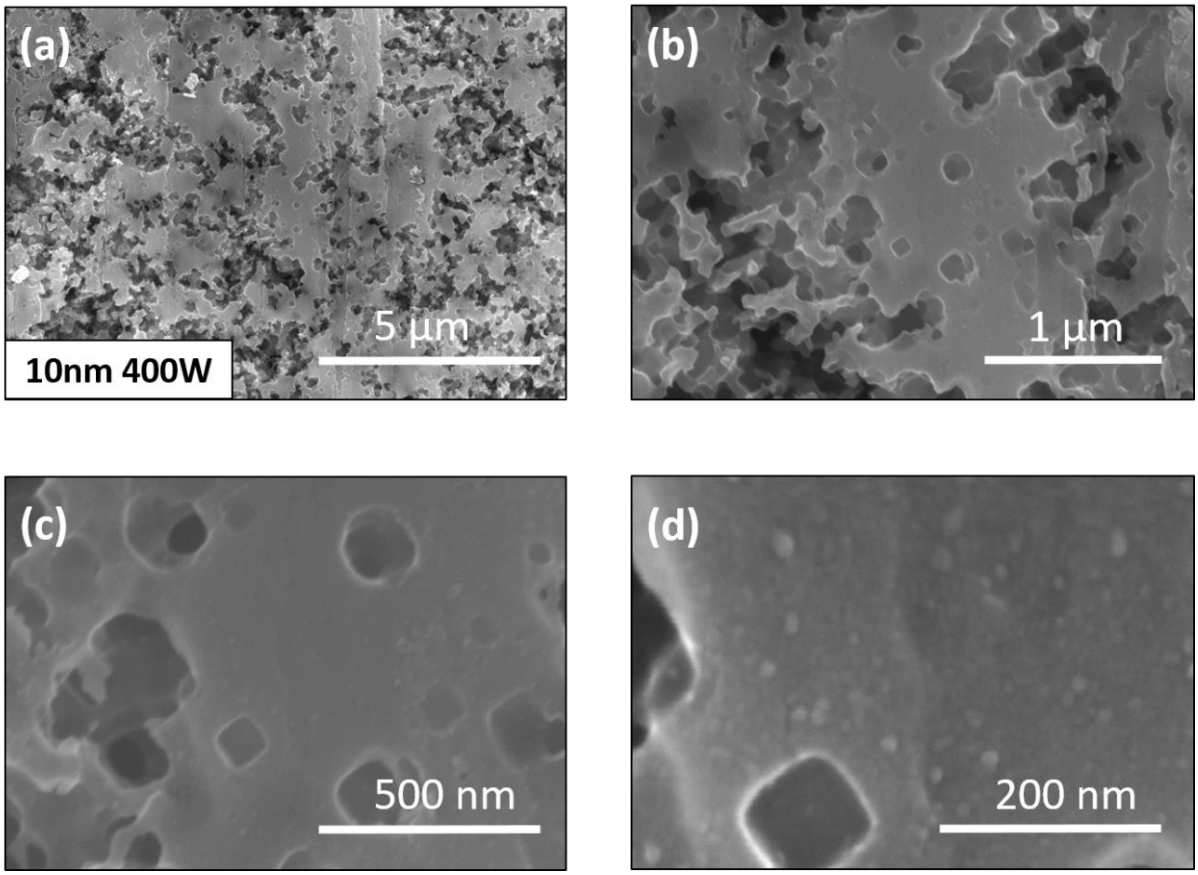

Figure 22: FESEM images - ***(a)****,* ***(b)****,* ***(c)****, and* ***(d)*** *represent the Al foil with 10 nm @ 400W (3.2Å/s) as-deposited Ni thin film.*

Using ImageJ software, an area of $88888.520\ nm^2$ was selected from the as-deposited Al foil surface (*presented as dashed rectangle in red in Fig 23a*) for analysis.

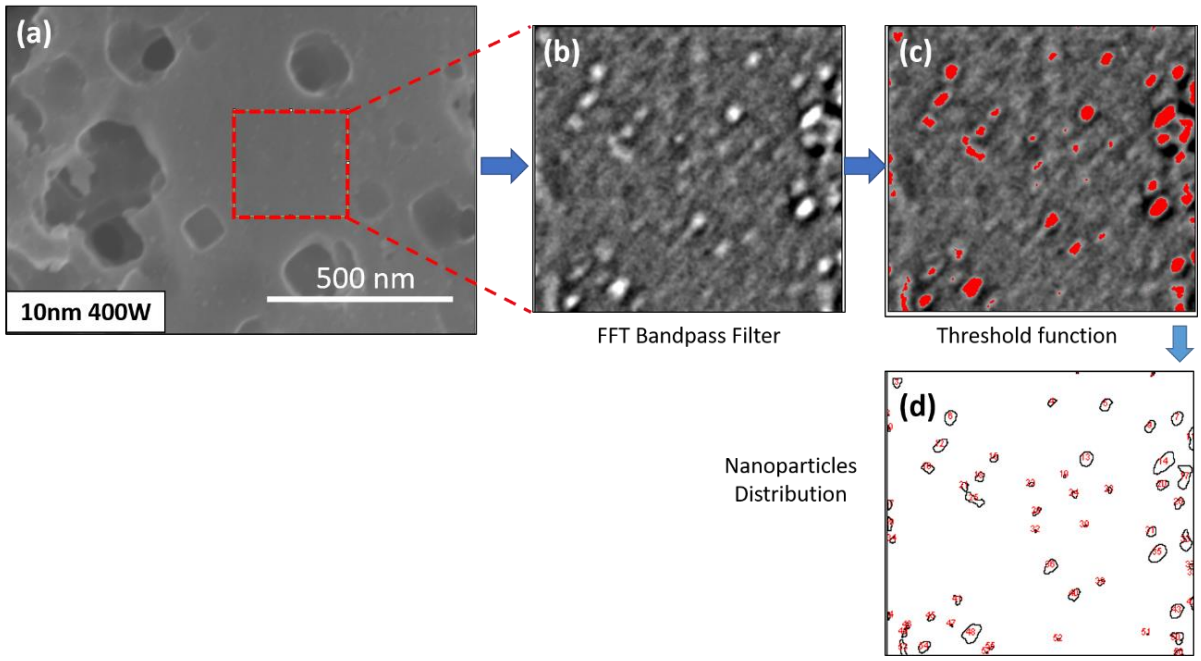

Figure 23: ***(a)*** *area selection,* ***(b)*** *FFT bandpass filter,* ***(c)*** *threshold function,* ***(d)*** *nanoparticles distribution.*

A comparison is presented in Table 4. The thin film thickness was fixed at 10 nm, while the applied power (*sputter rates*) that sputtered the target Ni material on the substrate was varied. As per the values obtained using analysis with ImageJ software, a smaller mean nanoparticle diameter was observed for the lowest power (*lowest sputtering rate*). Although the minimum nanoparticle diameter was the same for all applied power levels, the mean nanoparticle diameter was calculated to be 7.76, 8.05, and 8.95 nm for 25W (0.14 Å/s), 100W (0.77 Å/s), and 400W (3.2 Å/s) respectively. This is in agreement with the fact that faster sputtering rates lead to larger mean grain diameters [55]. This is also consistent with the fact that higher applied powers lead to the heating of the substrate and thus increase the adatom mobility. This higher adatom mobility leads to agglomeration of the nanoparticles and hence a larger mean diameter [56]. Another key observation was the gradual reduction in the spatial density of nanoparticles as the power was increased. This confirms that at higher powers, the adatom mobility gives rise to agglomeration which simply reduces the nanoparticle count.

Table 4: Thin film of 10 nm, influence of applied power over mean nanoparticle diameter among other parameters such as spatial density and surface coverage.

Applied Power (W)	Spatial Density (μm^{-2})	Surface Coverage (%)	Mean Nanoparticle Diameter (nm)	Maximum Nanoparticle Diameter (nm)	Minimum Nanoparticle Diameter (nm)
25W (0.14Å/s)	2032.41	9.62	7.76	21.64	1.11
100W (0.77Å/s)	1972.07	9.95	8.05	18.01	1.11
400W (3.2Å/s)	641.25	4.03	8.95	18.62	1.11

A similar analysis using ImageJ is not applicable to thin films of larger values i.e. 100 nm and 250 nm. The reason is that for larger thin films, the nanoparticles are sputtered on top of each other leading to coalescence and hence granular thin films are observed rather than nanostructured particles. This phenomenon can be confirmed from the observation of 100 nm and 250 nm thin films as in Figure 24. High surface coverage is observed. In view of this, a different approach was used which entailed the cross-sectional characterization of the thin films.

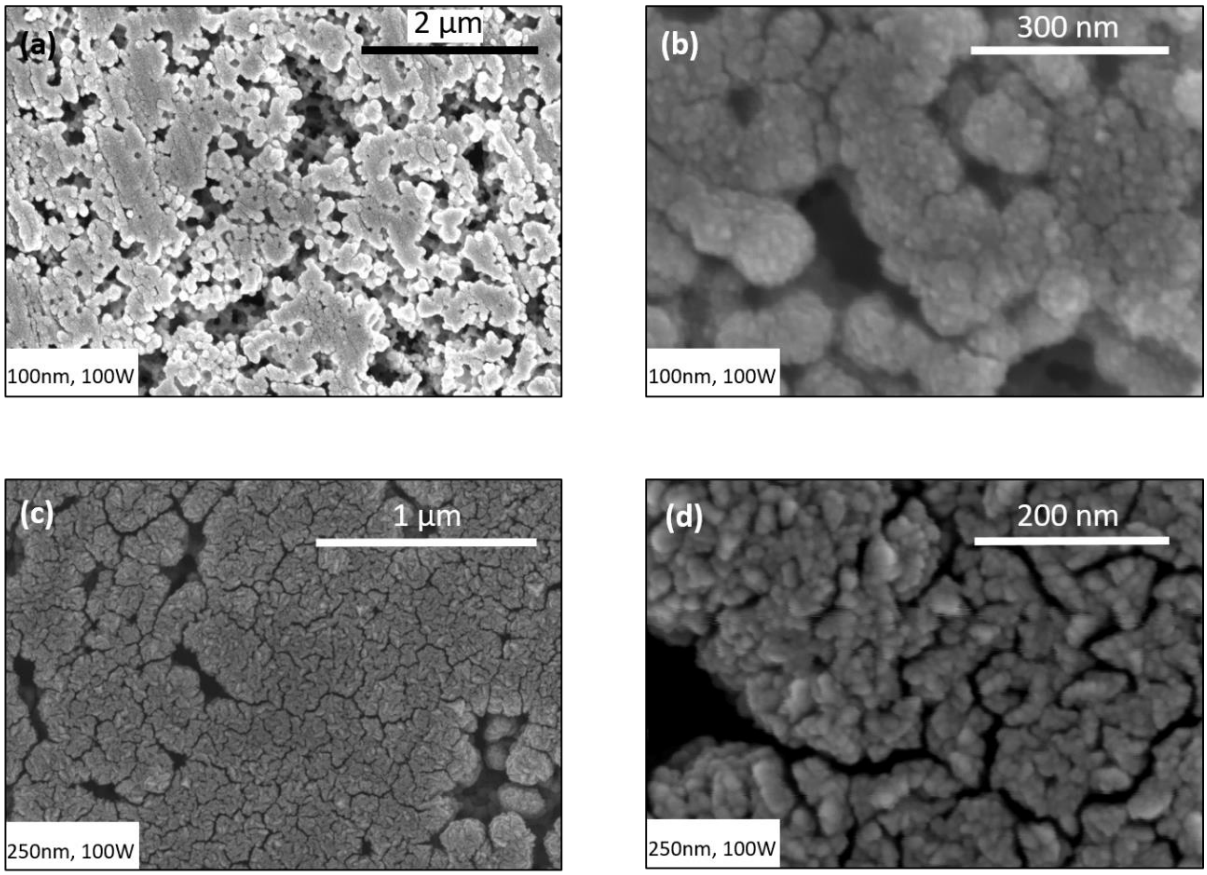

*Figure 24: FESEM images **(a)**, **(b)** show 100 nm and **(c)**, **(d)** 250 nm thin films that exhibit agglomeration and high surface coverage.*

4.2 Morphology and Distribution of Ni Clusters/Film – Cross-sectional View

To measure the size of Ni clusters, and also the effect of applied power on the penetration of Ni into the microstructured Al foil, cross-sectional characterization was performed. The results reveal that the Ni penetration into the porous foil increases with an increase in the applied power. This is in agreement with the theoretical understanding of the sputtering process, which establishes that when a higher power is applied, the argon atoms strike the target material i.e. Ni with a higher kinetic energy. This energy is then transferred into the sputtered target material which travels toward the substrate. This high energy allows the sputtered atom to penetrate the Al foil and reach deep inside compared to lower applied power levels.

A very thin, virtually indistinguishable 10 nm layer is presented in Figure 25(a), which upon further magnification (Figure 25d) reveals ~7.7 nm of Ni nanoparticles. This is in agreement with the findings of the top-view analysis conducted via the ImageJ software.

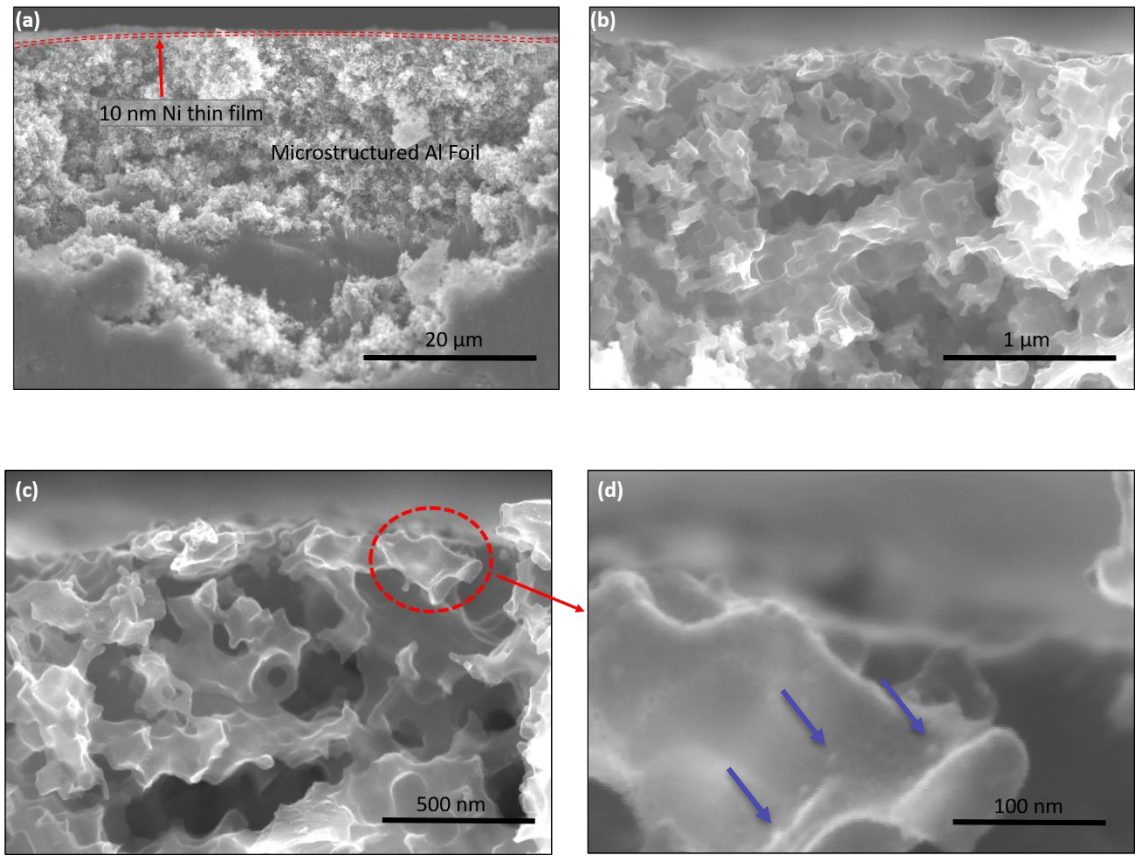

*Figure 25: FESEM images - **(a)**, **(b)** show the virtually indistinguishable 10 nm thin film deposited @ 100W (0.77Å/s), **(c)**, **(d)** feature magnified imagery with blue arrows pointing to nanoparticles.*

EDX mapping also confirms the presence of a very thin 10 nm Ni layer at the very surface of the Al foil. Distribution of Ni, O, and Al is presented in Figure 26.

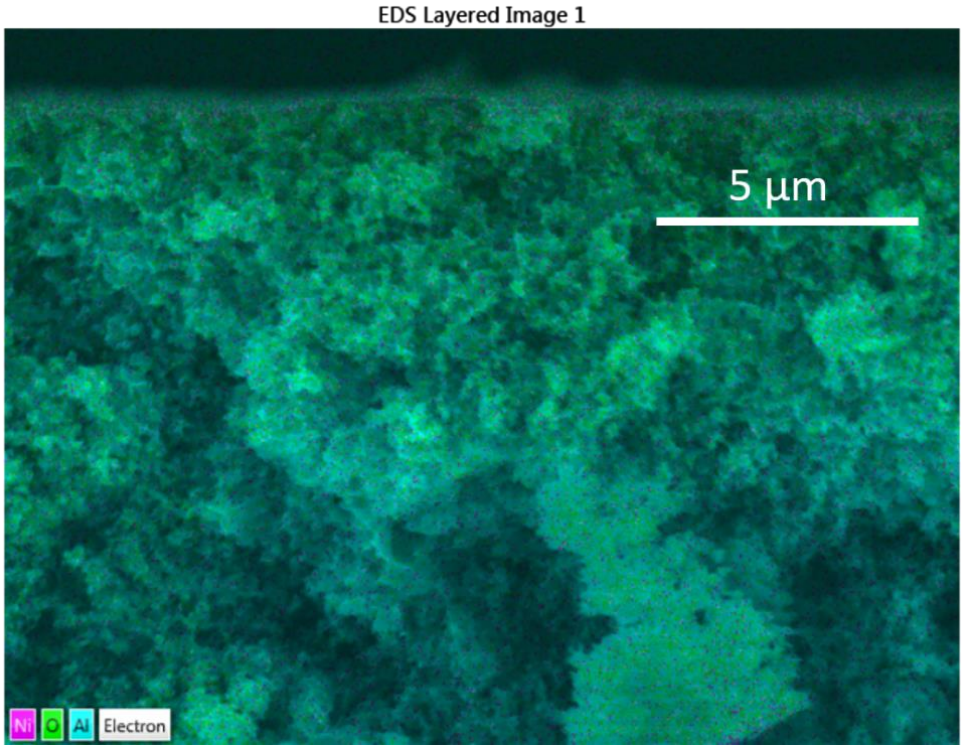

Figure 26: Scanned area of the as-deposited surface used for mapping.

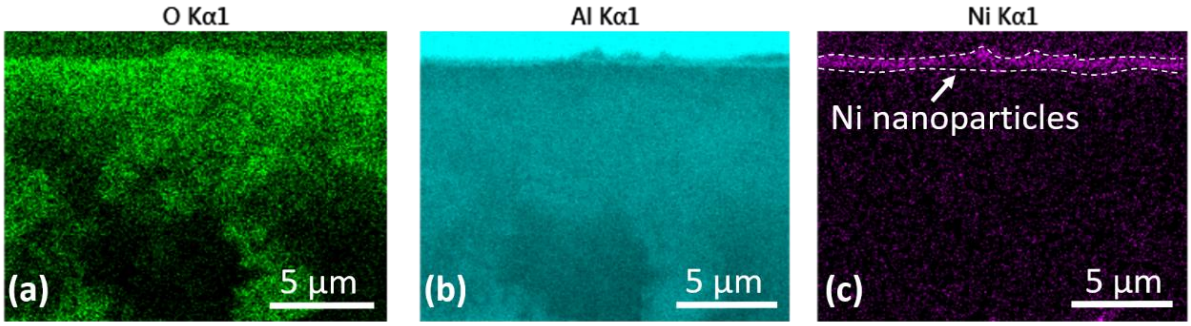

Figure 27: ***(a)***, ***(b)***, ***(c)*** *show the distribution and density of oxygen, aluminum, and nickel respectively.*

The applied power has a significant effect on the penetration of the Ni nanoparticles into the microstructured foil. This is presented in terms of the measured film thickness and cluster diameter.

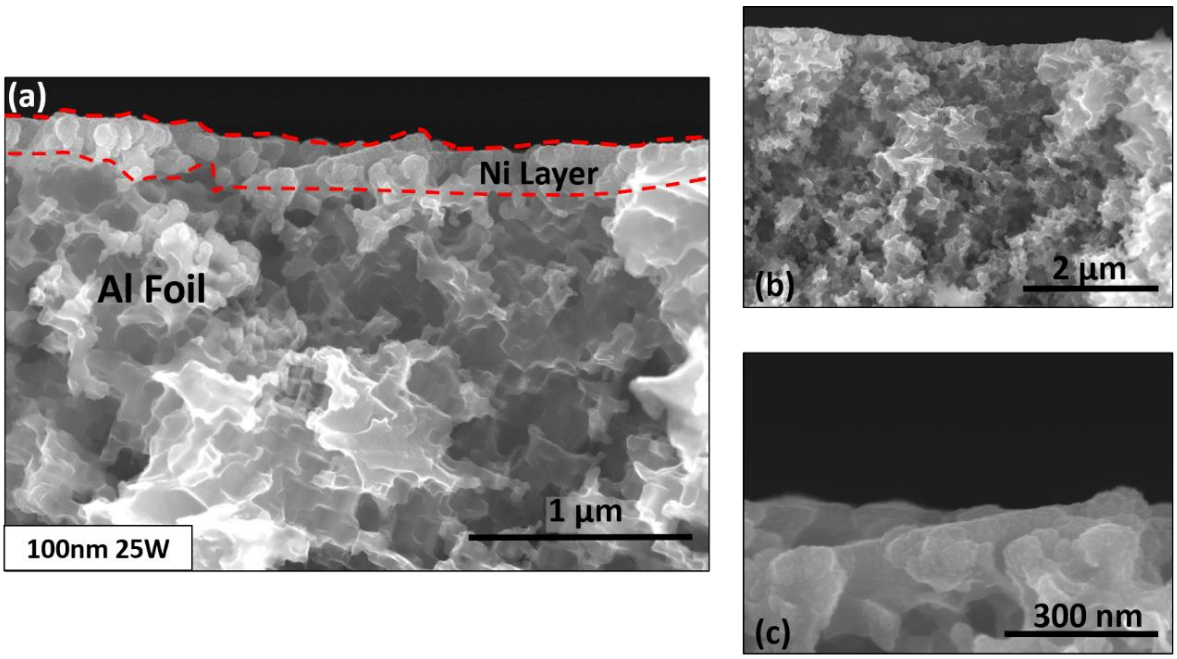

*Figure 28: FESEM images - **(a)** represents the thickness on the microstructured Al surface for 100 nm thin film deposited at 25W, **(b)** and **(c)** show the same area at different magnifications.*

Although the deposited film as per the QCM detector in Sputter AJA was only 100 nm, however, due to a non-planar surface, the film thickness as indicated in dashed red lines (Figure 28a) was averaged at 190.25 nm using the ImageJ software. To calculate this average value, measurements at four different points in the Figure 28a were taken using ImageJ software. This verifies the fact that the Ni material is able to seep into the microstructured foil even at lower powers such as 25W (0.14 Å/s). Similarly, an analysis of 100 nm thin film deposited at higher powers such as 100W (0.77 Å/s) and 400W (3.2 Å/s) revealed that the Ni nanoparticles were able to trickle even deeper inside the foil, and therefore larger measured film thicknesses were observed.

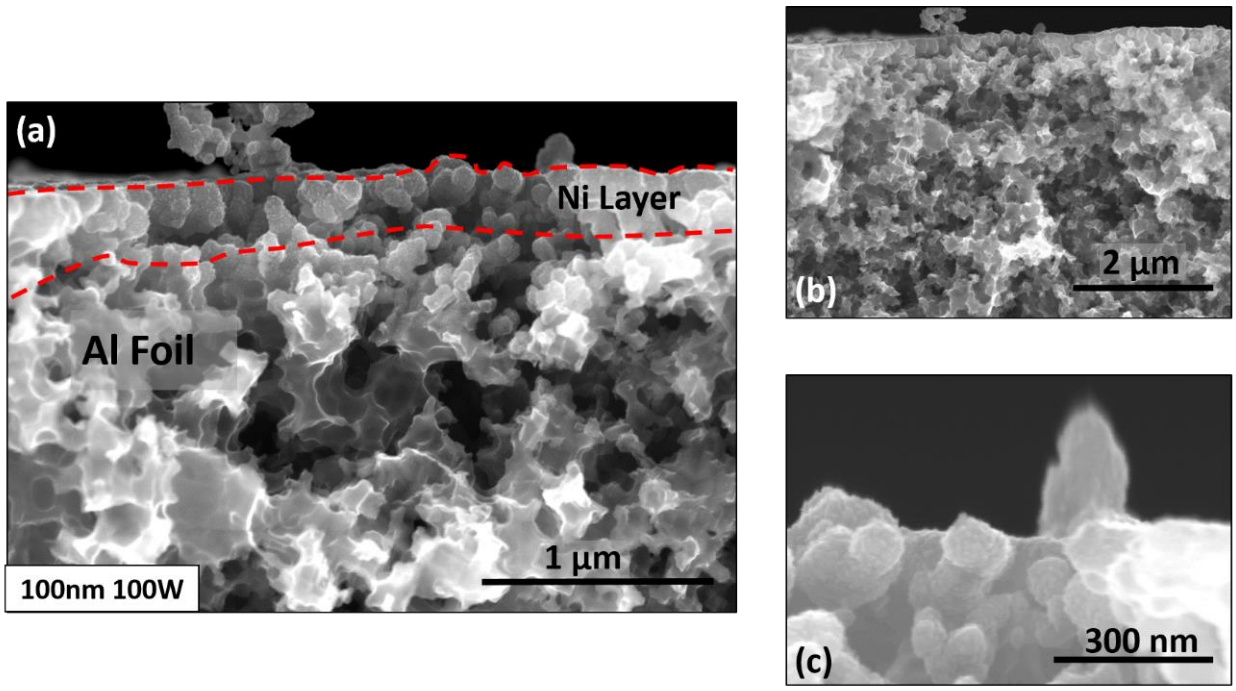

*Figure 29: FESEM images - **(a)** represents the thickness on the microstructured Al surface for 100 nm thin film deposited at 100W, **(b)** and **(c)** show the same area at different magnifications.*

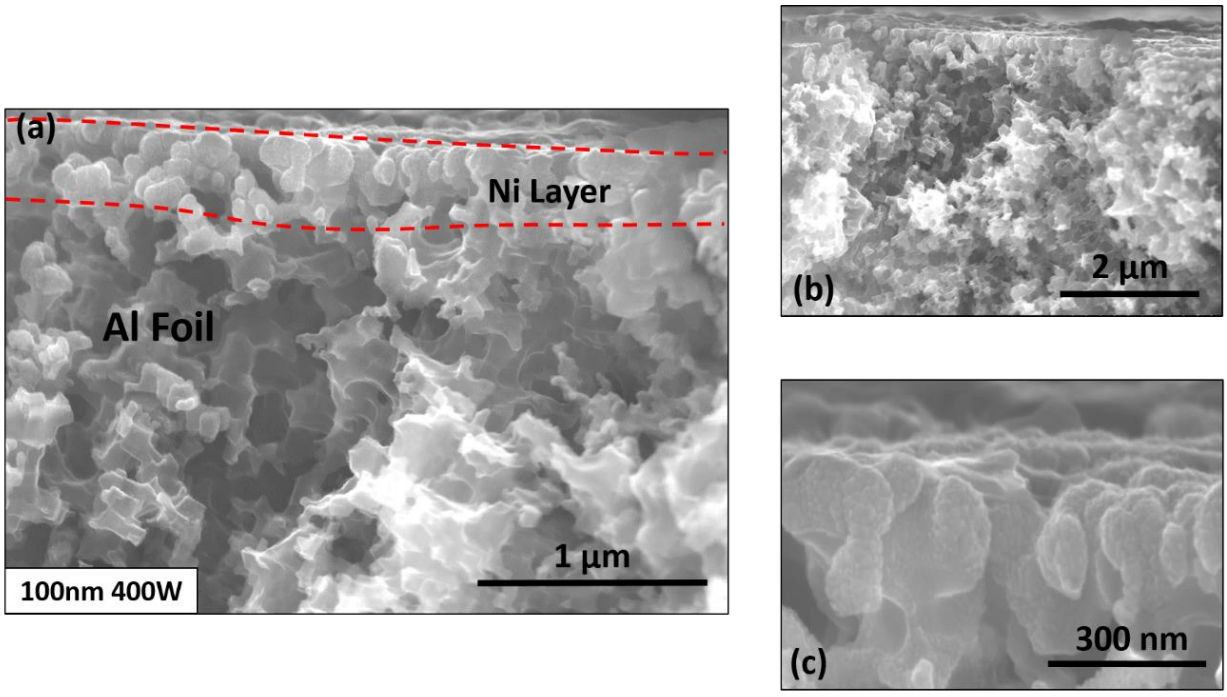

*Figure 30: FESEM images - **(a)** represents the thickness on the microstructured Al surface for 100 nm thin film deposited at 400W **(b)** and **(c)** show the same area at different magnifications.*

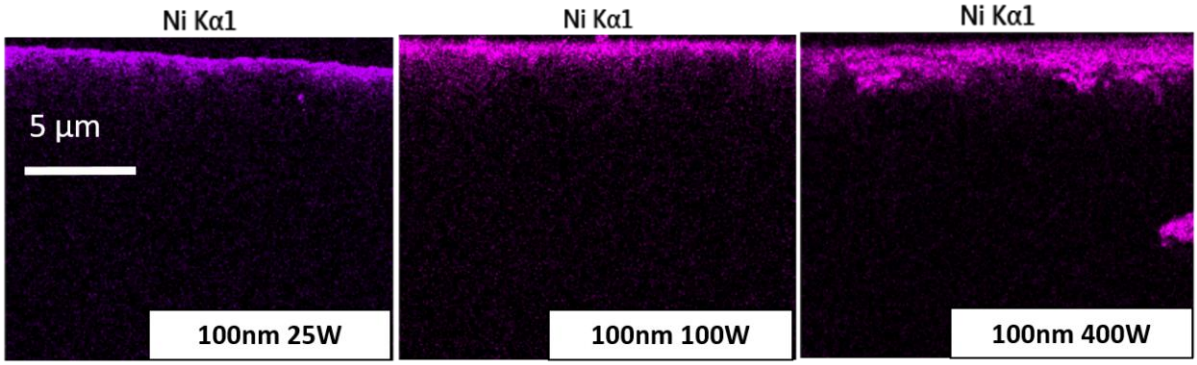

Figure 31: Depiction of the Ni layer for various powers (25W, 100W, and 400W) and the influence of applied power on the penetration depth of Ni into the microstructured Al substrate.

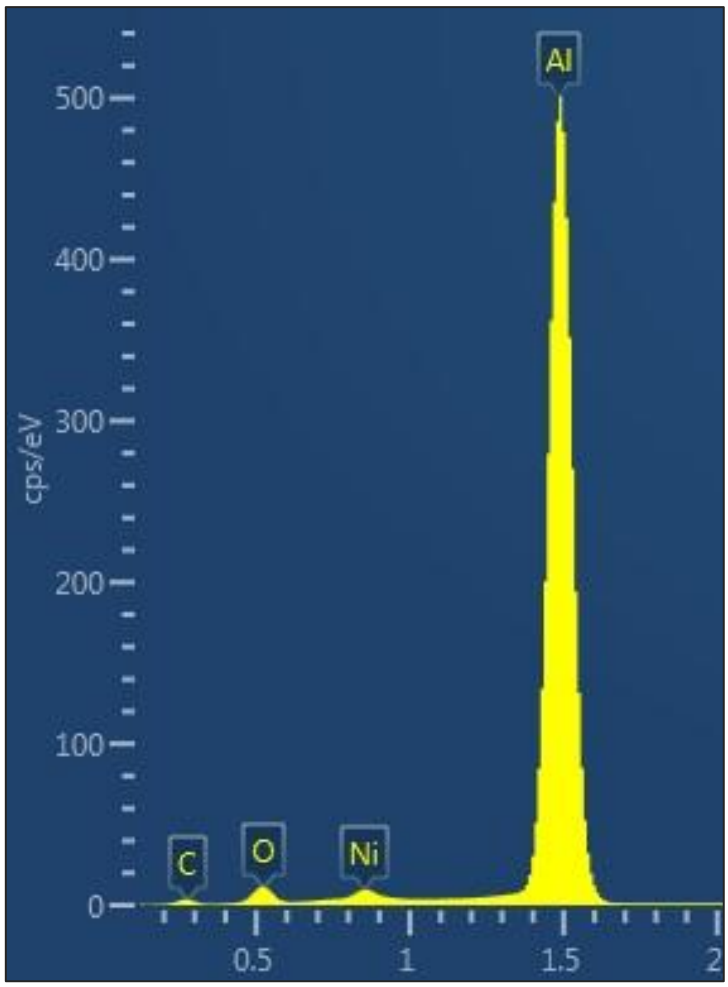

Figure 32: Spectrum confirming the presence of Ni.

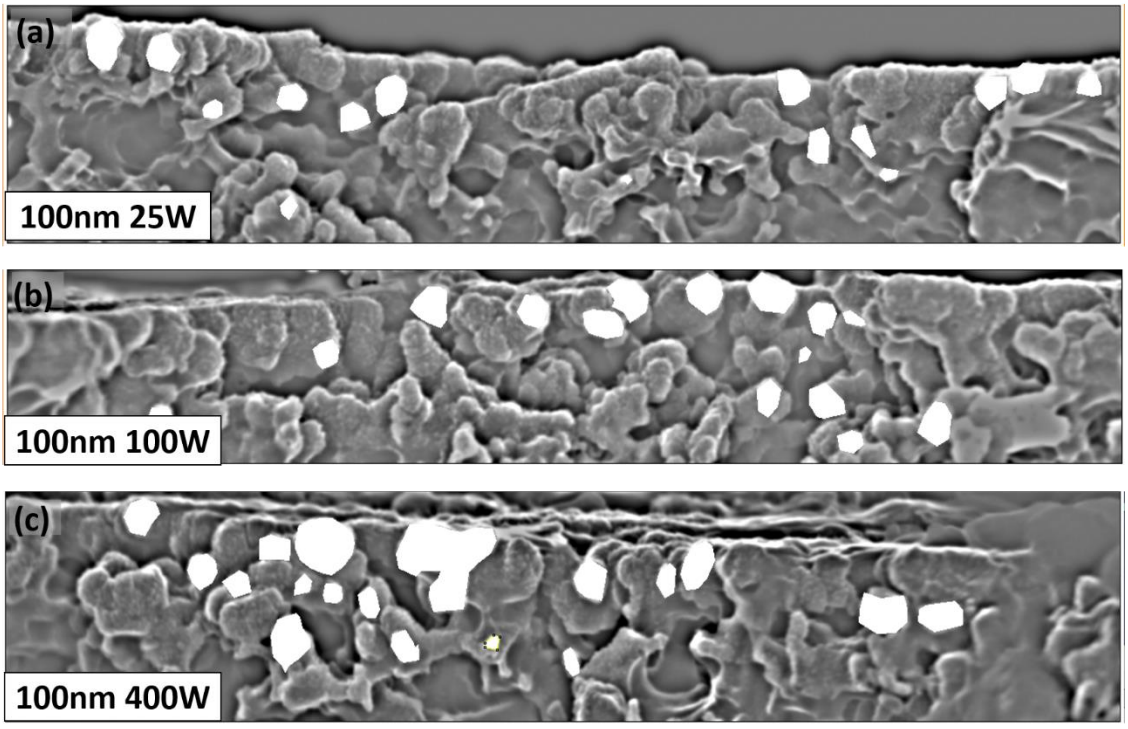

Figure 33: Shows the top part of the image containing clusters separated from the bottom microstructured part for analysis. White fillings indicate clusters having clear boundaries that were selected for measuring the diameter using ImageJ. ***(a)***, ***(b)***, ***(c)*** *represent 100 nm thin film deposited at various powers i.e. 25W, 100W, and 400W.*

The film thickness was measured by averaging four different points within the dashed red line in Figures 28 ,29, and 30, using the ImageJ software. For measuring the Ni cluster diameter, the top part i.e. Ni layer for the samples under observation was taken and then clusters having clearly defined boundaries were selected, and their average diameter was calculated. Table 5 presents the values of film thickness and Ni cluster diameter for the applied powers i.e. 25W, 100W, and 400W against the sputtered film thickness fixated at 100 nm.

Table 5: Measured film thickness and Ni cluster diameter are given with corresponding applied power levels.

Sputtered Film Thickness Fixed at 100 nm		
Power (W)	Measured Film Thickness (nm)	Ni Cluster Diameter (nm)
25	190.25	79.8
100	360	87.42
400	414	107.07

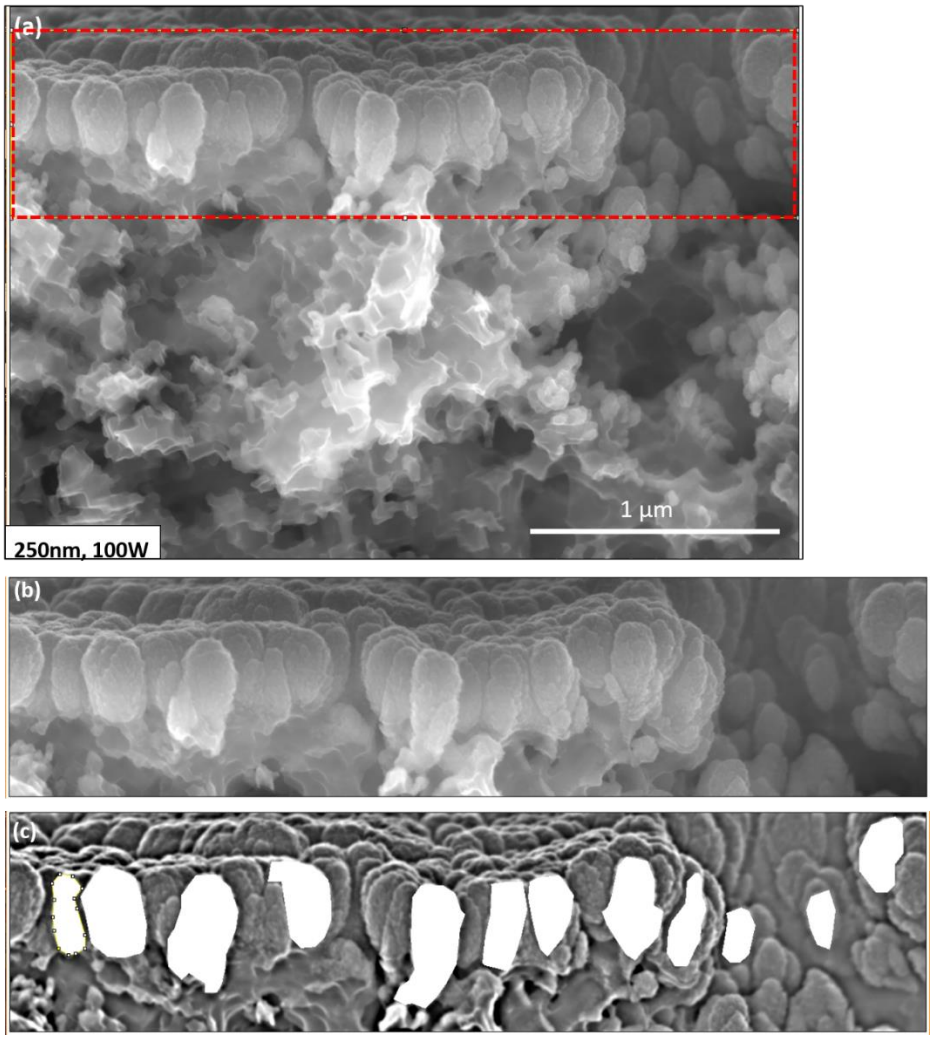

*Figure 34: **(a)** shows the Ni layer as clusters majorly concentrated on the top of the Al surface, **(b)** and **(c)** represent the analysis performed on the Ni clusters using ImageJ.*

The diameter of the Ni cluster (*represented as white fillings*) for 250 nm thin film sputtered at 100 W (0.77 Å/s) was calculated to be 217.10 nm, and the measured film thickness was found to be 354 nm.

4.2.1 Influence of heat treatment on the morphology and distribution of Ni Nanoparticles

The samples were subjected to heating at 600°C for 60 minutes inside the CVD reactor to study the evolution of the Ni nanoparticles in Ar environment. It was found that the nanoparticles under the influence of enhanced mobility resulted in coalescence leading to larger nanoparticle diameters. Figure 35 represents a 10 nm sample post heat treatment. As it can be observed, the nanoparticle diameters are larger than before heat treatment.

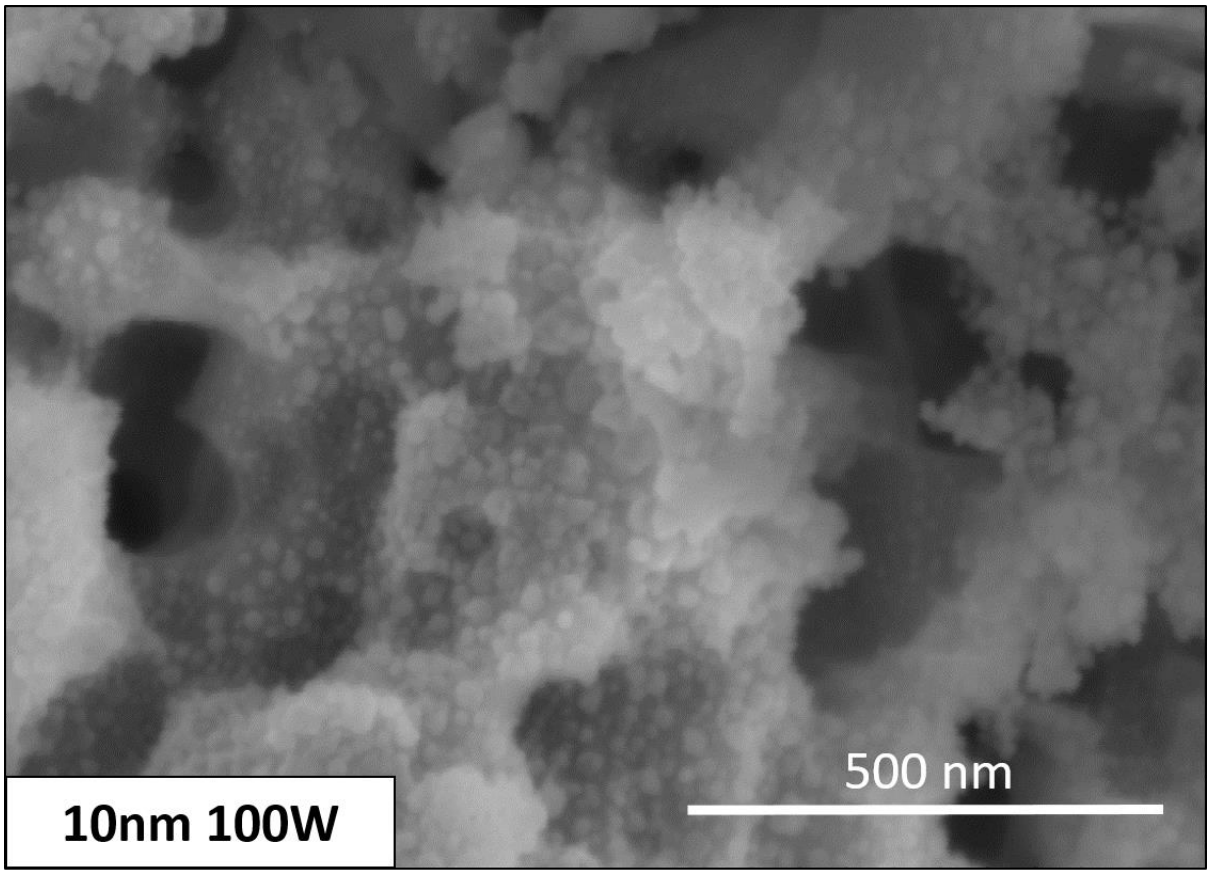

Figure 35: Shows the increase in the size of the Ni nanoparticles post heat treatment at 600˚C for 60 minutes in Ar environment.

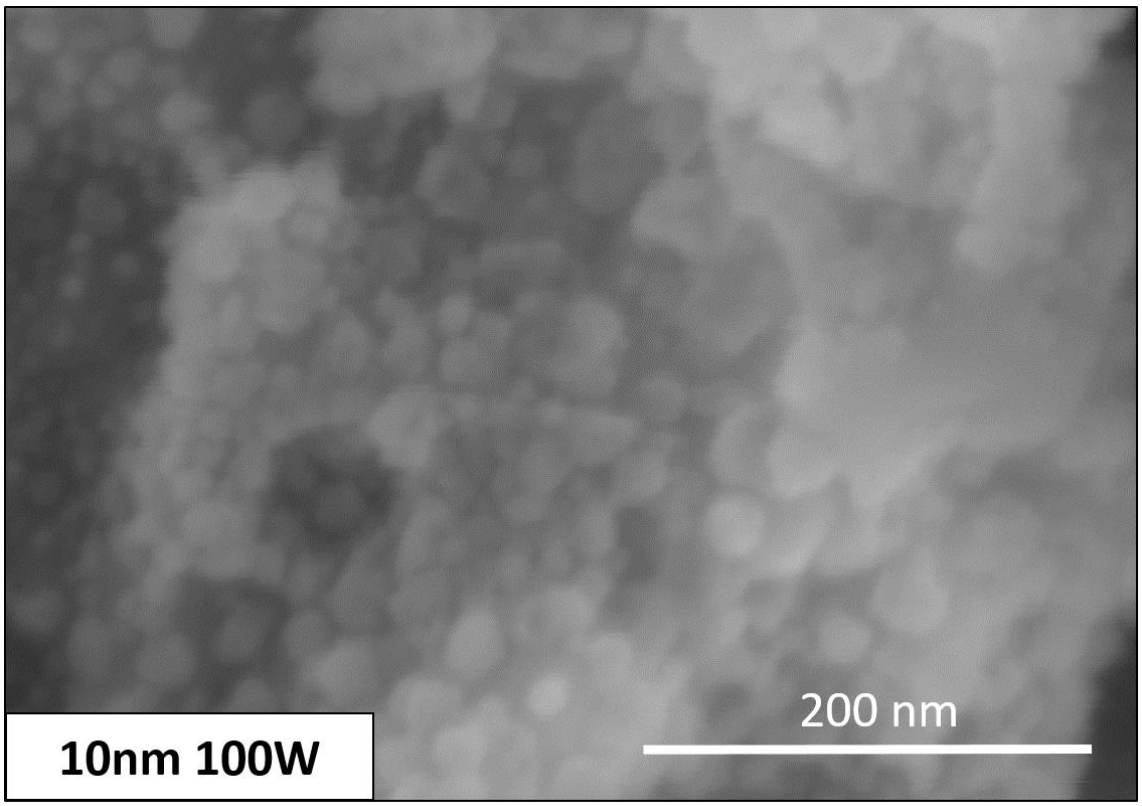

Figure 36: Magnified image of a 10nm thin film showing the increase in the size of the Ni nanoparticles post heat treatment at 600˚C for 60 minutes in Ar environment.

An analysis of thermally treated 10 nm thin film using ImageJ software (Figure 37) revealed ~1.7 times gain in mean nanoparticle diameter. The surface coverage also increased due to agglomeration, while the spatial density declined, again due to coalescence. The "maximum nanoparticle diameter" increased about 3.5X than before heating. This also explains large diameter CNTs even though the nanoparticles are measured at 7.76 nm. Corresponding values of spatial density, minimum nanoparticle diameter, and so on is presented in Table 6.

Another post heat treatment analysis using ImageJ software of 100 nm 100 W sample is presented in Figure 46 and a comparison of this is available in Table 10 in the Appendix.

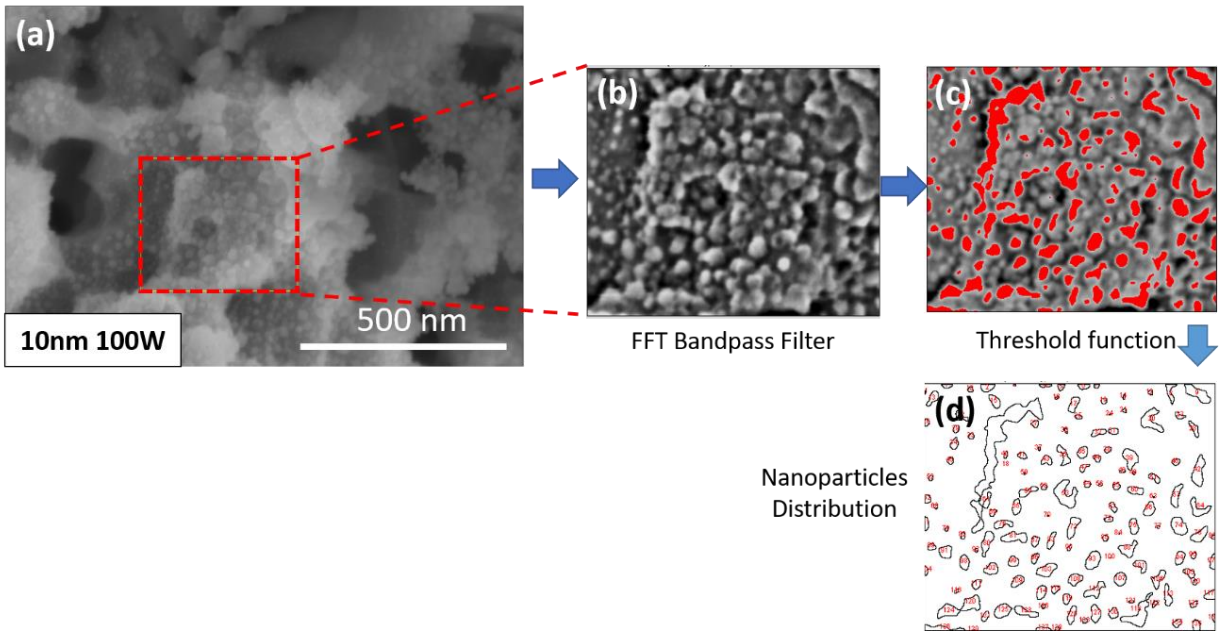

*Figure 37: **(a)** area selection, **(b)** FFT bandpass filter, **(c)** threshold function, **(d)** nanoparticles distribution.*

Table 6: Thin film of 10 nm after heat treatment at 600°C.

Applied Power	Spatial Density (μm^{-2})	Surface Coverage (%)	Mean Nanoparticle Diameter (nm)	Maximum Nanoparticle Diameter (nm)	Minimum Nanoparticle Diameter (nm)
100 (0.77Å/s)	1109.46	16	13.65	60.48	1.11

4.3 Characterization of Carbon Nanotubes (CNTs)

APCVD was performed on the most contrasting samples to study the influence of the Ni nanoparticle diameter, morphology and distribution on the grown CNTs. The power was fixed at 100 W (0.77 Å/s) and thin films of 10, 100 and 250 nm were chosen for CNT synthesis. It was observed that higher Ni films, specifically 250 nm, tend to result in a phenomenon called "peel off". Due to this, the CNTs appear to be flaky and exhibit weak adhesion. This is contributed by the stress caused by a high density of carbon nanotubes on the Al foil as well as the high temperature of 600˚C during the CVD process.

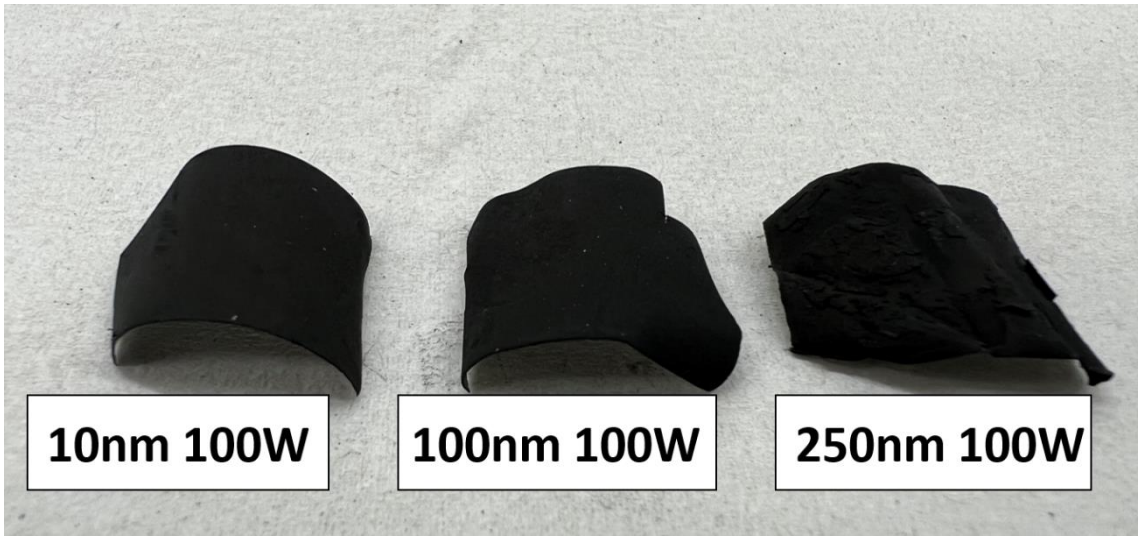

Figure 38: Carbon Nanotubes (CNTs) grown through CVD process

CNT carpet height was calculated by characterizing the cross-section of the as-grown samples. The carpet height of the CNT layer for 100 nm Ni film was found to be the highest among the samples studied. For 250 nm Ni thin film, the CNTs suffered from the "peel off" effect which led to CNTs falling off and therefore, a correct value of the carpet height was not possible to calculate. The CNT layer carpet height followed the sequence: 100 nm > 10 nm > 250 nm. Figures (39, 40, and 41) present the cross-sectional view of CNT synthesized samples with corresponding CNT carpet heights. A comparison of these is available in Table 7.

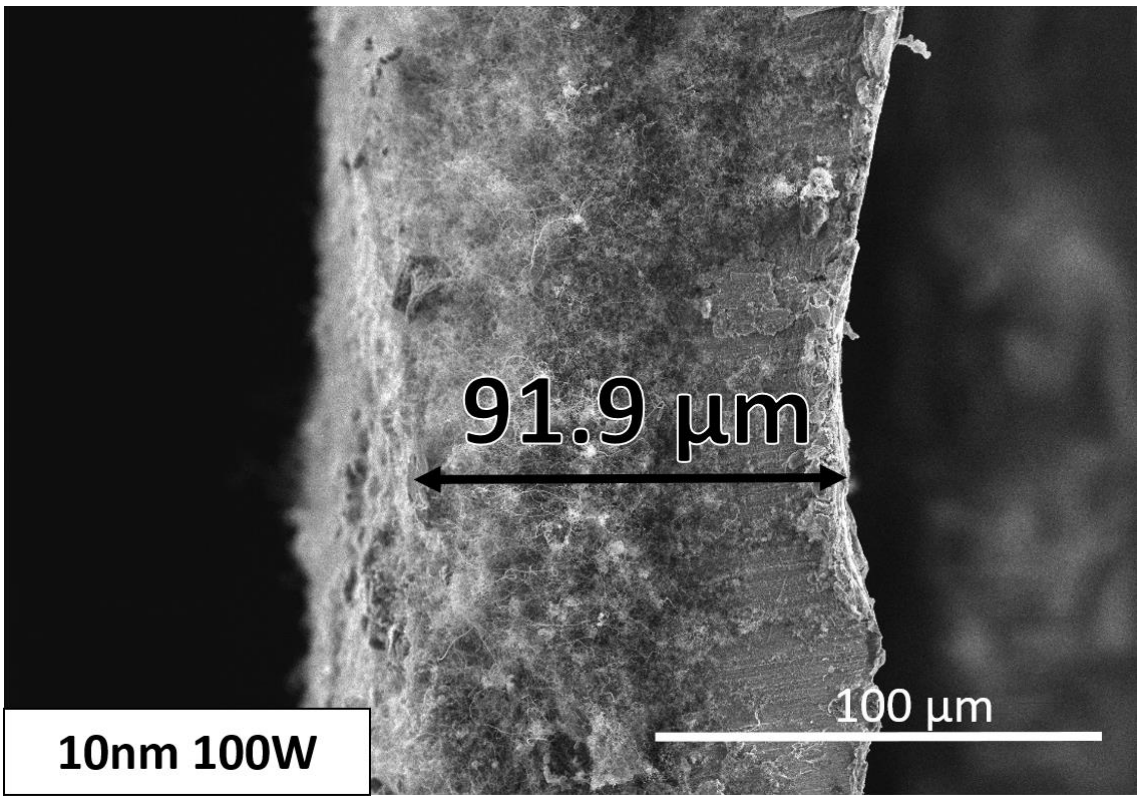

Figure 39: CNT carpet height for 10 nm sample.

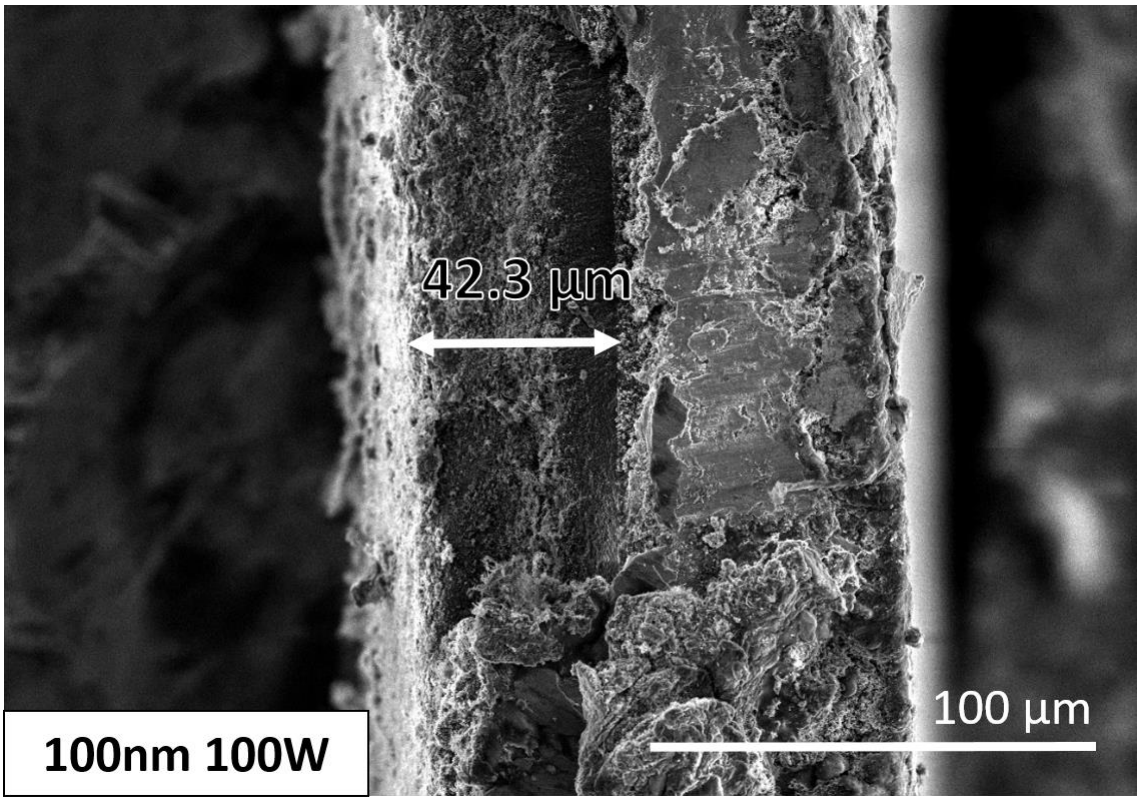

Figure 40: CNT carpet height for 100 nm sample.

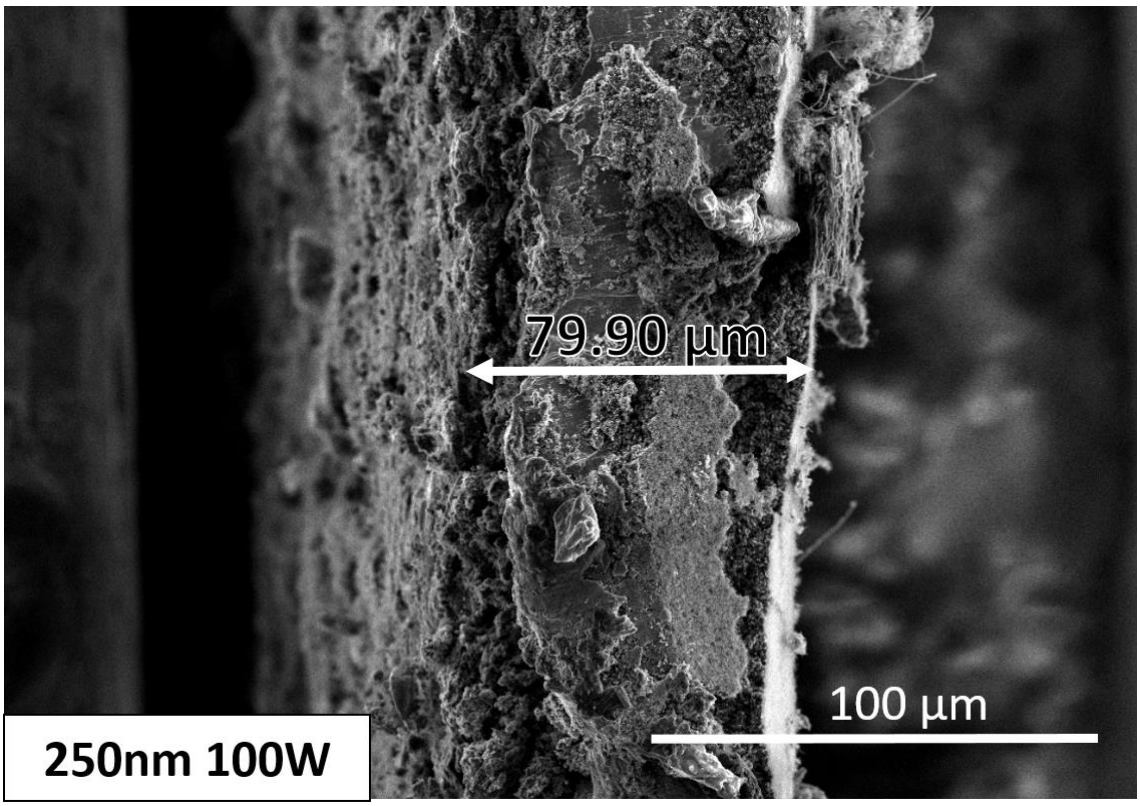

Figure 41: CNT carpet height for 250 nm sample.

Table 7: Comparison of CNT carpet height for different film thicknesses.

CNT Layer Carpet Height	
Ni Thin Film (nm)	Carpet Height (µm)
10	31.9
100	42.3
250	19

4.3.1 Influence of Ni Nanoparticle/Cluster Diameter on Carbon Nanotubes

The influence of Ni nanoparticle/cluster diameter on CNTs was studied. It was revealed that at higher powers, the CNTs possess a larger diameter. This is in agreement with the fact that Ni nanoparticles/clusters at higher powers tend to coalesce due to increased ad-atom mobility. Since the Ni nanoparticles/clusters get larger in diameter at higher powers (*due to self-heating of the substrate caused by high energy bombardment of target*

materials), thus the carbon nanotubes that grow out of these nanoparticles/clusters also possess a larger diameter. The CNT diameters range between 30 and 160 nm for all samples studied. However, the overall CNT diameter distribution is different and averaged values are provided in Table 8.

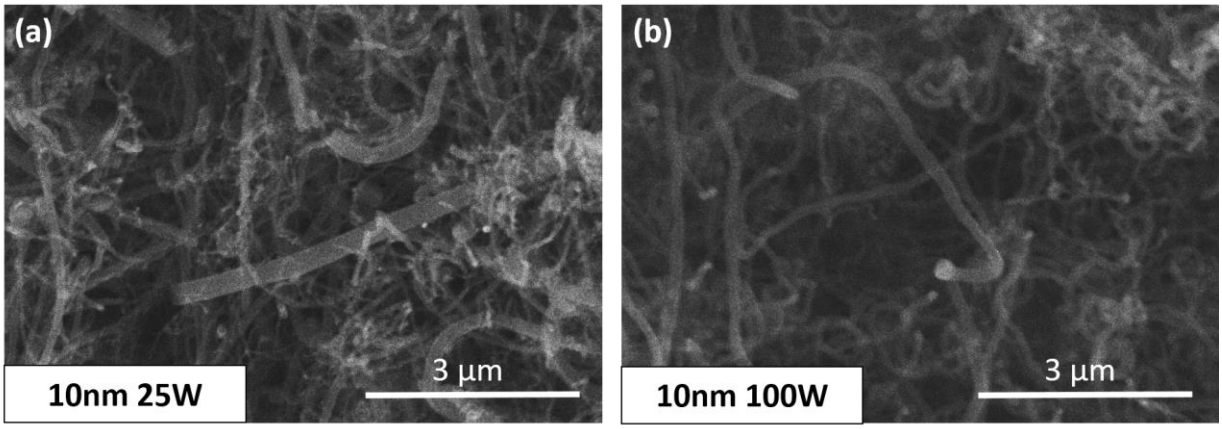

Figure 42: CNTs grown on 10 nm thin film. ***(a)*** *25W,* ***(b)*** *100W.*

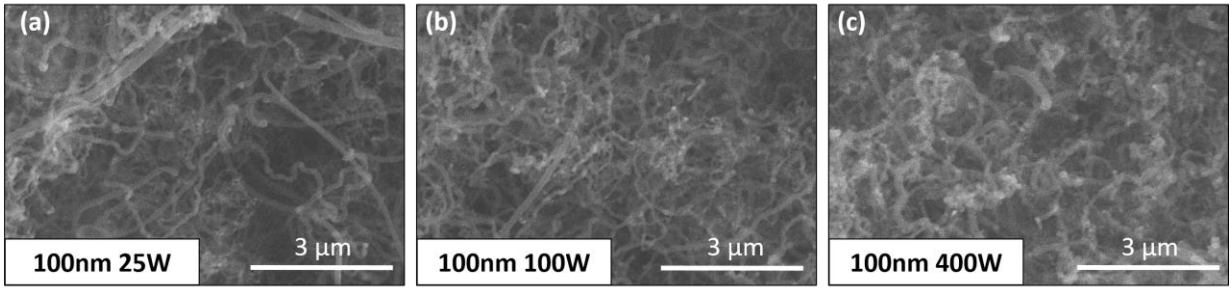

Figure 43: CNTs grown on 100 nm thin film. ***(a)*** *25W,* ***(b)*** *100W,* ***(c)*** *400W.*

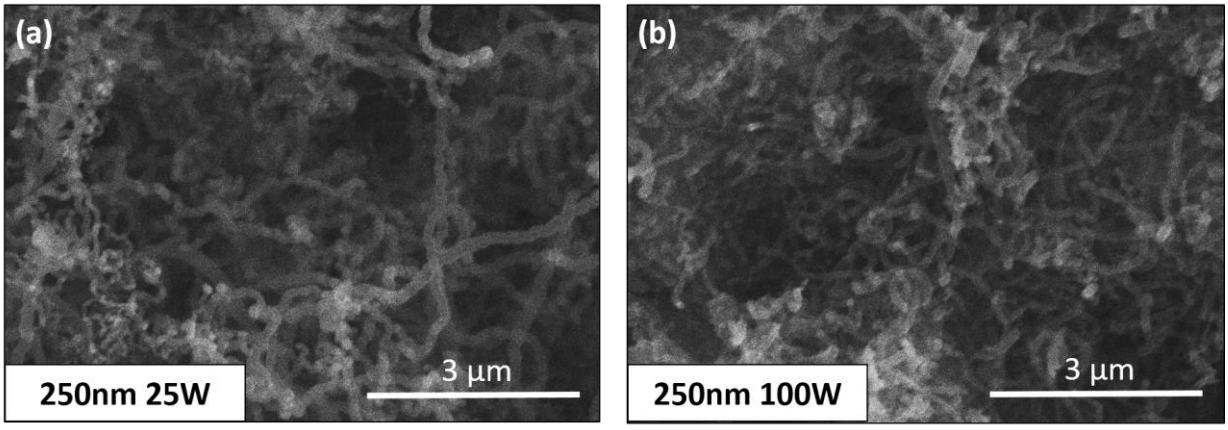

Figure 44: CNTs grown on 250 nm thin film. ***(a)*** *25W,* ***(b)*** *100W.*

Table 8 contains averaged values of the diameter of carbon nanotubes grown on three different values of Ni thin films (10, 100, and 250 nm) at different power levels (25, 100, and 400 W). It is clear that the CNT diameter increases with an increase in power.

Table 8: Comparison of CNT diameters due to changes in film thickness and applied power.

Ni thin film (nm)	Power (W)	Sputtering Rate (Å/s)	CNT Diameter (nm)
10	25	0.14	105.8
10	100	0.77	121.3
100	25	0.14	110
100	100	0.77	118
100	400	3.2	159.6
250	25	0.14	116.4
250	100	0.77	140.2

Another observation is the tip growth mechanism which is presented in Figure 45. This suggests weak adhesion between the Ni material and the Al substrate, which is understandable as sputter technique is non-conformal and the thin films coated via this method are majorly concentrated only at the top surface. A schematic of this phenomenon is presented in Figure 6.

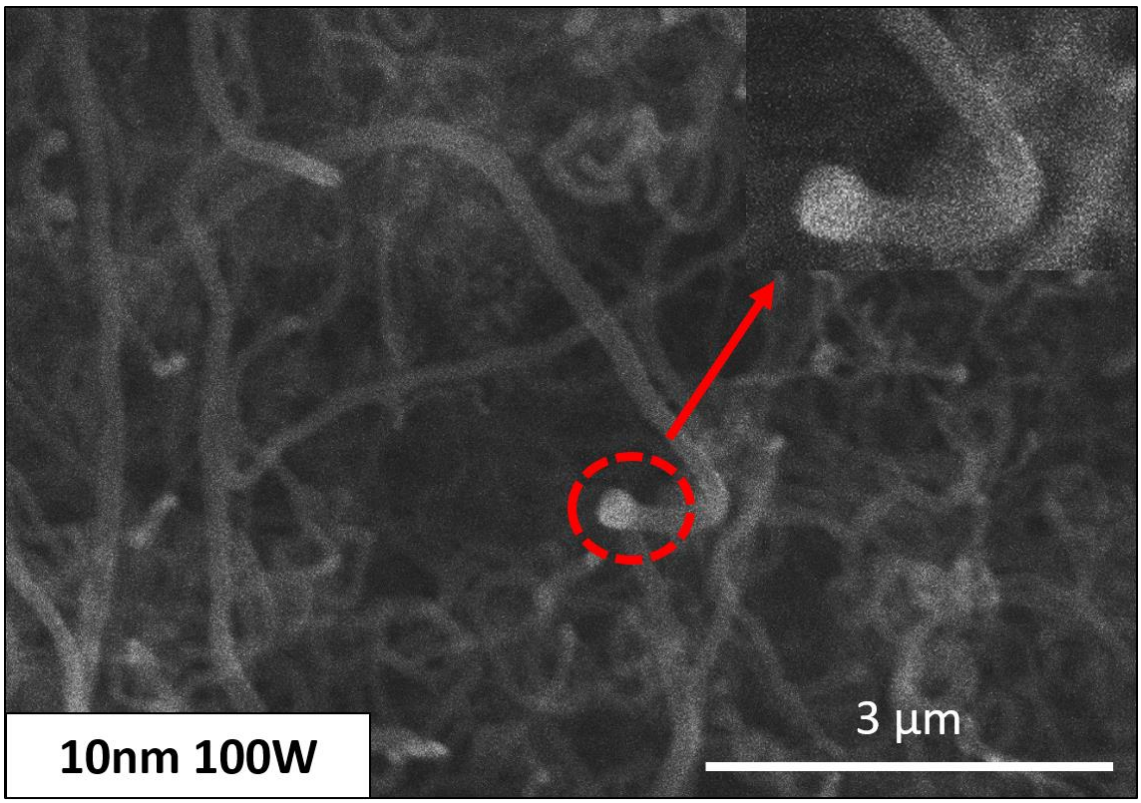

Figure 45: CNTs followed tip growth mechanism. Encircled part indicates Ni particle.

4.3.2 CNT Mass Loading

CNT mass loading was calculated using equation 3.4. The result was averaged and two observations were made, (i) – Higher film thickness yields higher CNT mass loading, (ii) – Higher powers (*faster sputtering rates*) lead to a reduction in CNT mass loading. The reason for this is that at higher powers, the sputtered material goes under coalescence and hence CNTs of larger diameter are seen. Therefore less number of CNTs can be packed in a given area leading to reduced CNT mass loading. Table 9 presents a comparison of CNT mass loading with Ni thin films and applied power.

Table 9: CNT Mass Loading.

Ni thin film (nm)	Power (W)	Sputter Rate (Å/s)	CNT Mass Loading $(\frac{mg}{cm^2})$
10	25	0.14	7.86
10	100	0.77	5.2
10	400	3.2	5.67

100	25	0.14	19
100	100	0.77	14.4
100	400	3.2	11.6
250	25	0.14	23.25
250	100	0.77	23.7
250	400	3.2	19.7

Since CNT mass loading is a measure of the quantity of carbon nanotubes within a given volume or mass, it is a crucial determinant of the capacitance and energy density in a supercapacitor. A higher mass loading value such as 23.7 $\frac{mg}{cm^2}$ indicates increased electrode surface area, and in turn increased number of electrochemical reactions occuring at the electrode-electrolyte interface, which cause an improvement in charge storage.

5 Conclusion

5.1 Main Conclusion

The thesis concludes that the CNT mass loading increases with an increase in Ni film thickness, albeit at lower sputter deposition powers (*lower sputtering rates*). This increase in CNT mass loading can be extrapolated to make a comment on the energy density of supercapacitors as well. Since high CNT mass loading (i) - increases the available electrode surface area which contributes to a higher capacitance, (ii) - enhances the electrode-electrolyte interface, enhancing the number of charge storage sites to improve capacitance, and (iii) – improves electrical conductivity of the electrode material to facilitate charge transport and reduces internal resistance for enabling faster charge/discharge rates, therefore it can be concluded that the energy density of the supercapacitor can be improved using Ni films of higher thickness values sputtered at lower deposition rates. CNT mass loading of 7.86, 19, and 23.25 $\frac{mg}{cm^2}$ was calculated for thin films of 10, 100, and 250 nm respectively with power fixed at 25 W. The increase in power in this case proved counterproductive for mass loading, where a spike in applied power reduced the CNT mass loading. Highest CNT mass loading is achieved with thin films of 250 nm, and the values are 23.25 and 23.7 $\frac{mg}{cm^2}$ at 25 W and 100 W respectively.

Magnetron sputtering was found to be a non-conformal (*directional*) deposition process which did not utilize the entire porous Al material, and the majority of the Ni film was observed concentrated as the top layer only at the surface, with only a small number of nanoparticles present throughout the enlarged available surface area. This was confirmed using EDX mapping which showed Ni was concentrated only at the top. This non-conformal deposition led to a weak adhesion between the Ni material and the substrate, causing tip growth in the synthesized CNTs using CVD. A schematic of this is presented in Figure 6.

10 nm films, irrespective of the power (*or sputter rate*) at which these were sputtered on the substrate, presented a discontinuous growth and appeared as nanoparticles. Thin discontinuous films beyond 10 nm i.e. 100 and 250 nm appeared as continuous films exhibiting columnar growth as clusters at all applied power levels. Nanoparticles

measuring between 7.76 and 8.95 nm (*increase based on applied power*) were observed with thin film of 10 nm. Clusters ranging between 79.8 and 217.10 nm in diameter were measured for thin films of 100 and 250 nm. The spatial density decreased with an increase in power, which is consistent with our understanding of agglomeration and how the number of nanoparticles reduce simply because of coalescence.

The heat treatment of 10 nm thin film caused the nanoparticles diameter to increase from 8.05 nm to 13.65 nm, while at the same time the spatial density decreased from 1972.07 to 1109.46 μm^{-2} due to enhanced adatom mobility causing coalescence at higher temperatures. Similarly, surface coverage increased from 9.95% to 16% due to the same reason.

The penetration of Ni nanoparticles/clusters was found to increase with an increase in applied sputter power. This is because the ejected atoms bombarded the porous substrate with a higher kinetic energy and thus penetrated deeper. Larger film thickness also resulted in giving the overall impression of a higher penetration depth. A 100 nm thin film deposited via the sputter equipment which is optimized for planar surfaces such as Si wafer, reflected to be of 190.25, 360, and 414 nm at powers of 25, 100, and 400 W respectively on a non-planar, microstructured substrate i.e. the Al foil used for experiments.

The CNT diameter exhibited a direct relation with the NP/cluster diameter. It increased with an increase in the nanoparticle/cluster diameter. Mean CNT diameters of 105.8, 110, and 116.4 nm were observed for thin films of 10, 100, and 250 nm respectively with power fixed at 25 W.

CNTs grown on 10 nm and 100 nm sputtered samples were found to exhibit stronger adhesion compared to the ones on 250 nm samples. Since stronger adhesion promotes a reduction in equivalent series resistance (ESR), it can be argued to provide high storage capacity.

5.2 Future Work

There are many possibilities regarding future work related to this topic. Many more investigations can be carried out to test and improve the capacitance and energy density of the supercapacitors. Some of these are shortlisted as follows:

1. The possibility of modification of distance between the substrate and target material inside the sputter AJA deposition chamber. The current setup only provides for a substrate to target distance (STD) of 14-18 cm. A short distance (<7.5 cm) is considered suitable for forming nanostructured particles at lower powers. If modification down to 7.5 cm is not possible, there are still research opportunities available to investigate the size, morphology and distribution of the Ni particles by varying the STD within the available range.
2. The sputtering pressure or the argon flow can be varied to study the effect of mean free path (MFP) on the size, morphology and distribution of the Ni nanoparticles and thin films.
3. Thin films between 5 nm and 50 nm can be chosen to study the evolution of the Ni nanoparticles and a conclusion can be drawn as to, at what thickness does nanostructured, discontinuous films become granular/continuous films.
4. Even lower applied powers (*sputtering rates*) can be researched such as 10 W to study their effect on the size, morphology and distribution of the Ni nanoparticles.
5. Conformal deposition techniques such as dip coating, drop-coating, or evaporation can be utilized to adequately coat and fill the porous substrate with Ni. This is a reasonable option to utilize the enlarged surface area of the microstructured substrate for energy density improvement as well as to improve adhesion of the nanoparticles to the substrate.

All of the above discussed suggestions can be researched to improve the capacitance and energy density of supercapacitors.

References

[1] B. E. Conway, *Electrochemical Supercapacitors*. Boston, MA: Springer US, 1999. doi: 10.1007/978-1-4757-3058-6.

[2] A. S. Aricò, P. Bruce, B. Scrosati, J.-M. Tarascon, and W. Van Schalkwijk, "Nanostructured materials for advanced energy conversion and storage devices," *Nat. Mater.*, vol. 4, no. 5, pp. 366–377, May 2005, doi: 10.1038/nmat1368.

[3] R. J. Kuhns and G. H. Shaw, *Navigating the Energy Maze*. Cham: Springer International Publishing, 2018. doi: 10.1007/978-3-319-22783-2.

[4] S. Chu, Y. Cui, and N. Liu, "The path towards sustainable energy," *Nat. Mater.*, vol. 16, no. 1, pp. 16–22, Jan. 2017, doi: 10.1038/nmat4834.

[5] M. Tvaronavičienė, J. Baublys, J. Raudeliūnienė, and D. Jatautaitė, "Global energy consumption peculiarities and energy sources," in *Energy Transformation Towards Sustainability*, Elsevier, 2020, pp. 1–49. doi: 10.1016/B978-0-12-817688-7.00001-X.

[6] S. Bose, T. Kuila, A. K. Mishra, R. Rajasekar, N. H. Kim, and J. H. Lee, "Carbon-based nanostructured materials and their composites as supercapacitor electrodes," *J Mater Chem*, vol. 22, no. 3, pp. 767–784, 2012, doi: 10.1039/C1JM14468E.

[7] S. L. Candelaria *et al.*, "Nanostructured carbon for energy storage and conversion," *Nano Energy*, vol. 1, no. 2, pp. 195–220, Mar. 2012, doi: 10.1016/j.nanoen.2011.11.006.

[8] L. L. Zhang and X. S. Zhao, "Carbon-based materials as supercapacitor electrodes," *Chem. Soc. Rev.*, vol. 38, no. 9, p. 2520, 2009, doi: 10.1039/b813846j.

[9] M. A. Azam, A. Fujiwara, and T. Shimoda, "Significant Capacitance Performance of Vertically Aligned Single-Walled Carbon Nanotube Supercapacitor by Varying Potassium Hydroxide Concentration," *Int J Electrochem Sci*, vol. 8, 2013.

[10] M. D. Stoller, S. Park, Y. Zhu, J. An, and R. S. Ruoff, "Graphene-Based Ultracapacitors," *Nano Lett.*, vol. 8, no. 10, pp. 3498–3502, Oct. 2008, doi: 10.1021/nl802558y.

[11] H. Zhang, G. Cao, Y. Yang, and Z. Gu, "Comparison Between Electrochemical Properties of Aligned Carbon Nanotube Array and Entangled Carbon Nanotube Electrodes," *J. Electrochem. Soc.*, vol. 155, no. 2, p. K19, 2008, doi: 10.1149/1.2811864.

[12] W. Raza *et al.*, "Recent advancements in supercapacitor technology," *Nano Energy*, vol. 52, pp. 441–473, Oct. 2018, doi: 10.1016/j.nanoen.2018.08.013.

[13] A. González, E. Goikolea, J. A. Barrena, and R. Mysyk, "Review on supercapacitors: Technologies and materials," *Renew. Sustain. Energy Rev.*, vol. 58, pp. 1189–1206, May 2016, doi: 10.1016/j.rser.2015.12.249.

[14] T. Funabashi, "Introduction," in *Integration of Distributed Energy Resources in Power Systems*, Elsevier, 2016, pp. 1–14. doi: 10.1016/B978-0-12-803212-1.00001-5.

[15] R. Kavian, A. Vicenzo, and M. Bestetti, "Growth of carbon nanotubes on aluminium foil for supercapacitors electrodes," *J. Mater. Sci.*, vol. 46, no. 5, pp. 1487–1493, Mar. 2011, doi: 10.1007/s10853-010-4950-1.

[16] Z. Song, J. Hou, H. Hofmann, J. Li, and M. Ouyang, "Sliding-mode and Lyapunov function-based control for battery/supercapacitor hybrid energy storage system used in electric vehicles," *Energy*, vol. 122, pp. 601–612, Mar. 2017, doi: 10.1016/j.energy.2017.01.098.

[17] M. G. Carignano, R. Costa-Castelló, V. Roda, N. M. Nigro, S. Junco, and D. Feroldi, "Energy management strategy for fuel cell-supercapacitor hybrid vehicles based on

prediction of energy demand," *J. Power Sources*, vol. 360, pp. 419–433, Aug. 2017, doi: 10.1016/j.jpowsour.2017.06.016.
[18] F. Ali *et al.*, "Silicon-doped hafnium oxide anti-ferroelectric thin films for energy storage," *J. Appl. Phys.*, vol. 122, no. 14, p. 144105, Oct. 2017, doi: 10.1063/1.4989908.
[19] L. L. Zhang and X. S. Zhao, "Carbon-based materials as supercapacitor electrodes," *Chem. Soc. Rev.*, vol. 38, no. 9, p. 2520, 2009, doi: 10.1039/b813846j.
[20] C. Zhang, "Super pseudocapacitors," *Nat. Energy*, vol. 3, no. 12, pp. 1019–1019, Dec. 2018, doi: 10.1038/s41560-018-0301-2.
[21] A. Muzaffar, M. B. Ahamed, K. Deshmukh, and J. Thirumalai, "A review on recent advances in hybrid supercapacitors: Design, fabrication and applications," *Renew. Sustain. Energy Rev.*, vol. 101, pp. 123–145, Mar. 2019, doi: 10.1016/j.rser.2018.10.026.
[22] H. Dai, "Carbon nanotubes: opportunities and challenges," *Surf. Sci.*, vol. 500, no. 1–3, pp. 218–241, Mar. 2002, doi: 10.1016/S0039-6028(01)01558-8.
[23] K. Koziol *et al.*, "High-Performance Carbon Nanotube Fiber," *Science*, vol. 318, no. 5858, pp. 1892–1895, Dec. 2007, doi: 10.1126/science.1147635.
[24] M. S. Dresselhaus, G. Dresselhaus, and R. Saito, "C60-related tubules," *Solid State Commun.*, vol. 84, no. 1–2, pp. 201–205, Oct. 1992, doi: 10.1016/0038-1098(92)90325-4.
[25] J.-P. Issi, L. Langer, J. Heremans, and C. H. Olk, "Electronic properties of carbon nanotubes: Experimental results," *Carbon*, vol. 33, no. 7, pp. 941–948, 1995, doi: 10.1016/0008-6223(95)00023-7.
[26] T. W. Ebbesen, H. J. Lezec, H. Hiura, J. W. Bennett, H. F. Ghaemi, and T. Thio, "Electrical conductivity of individual carbon nanotubes," *Nature*, vol. 382, no. 6586, pp. 54–56, Jul. 1996, doi: 10.1038/382054a0.
[27] G. P. Gakis, S. Termine, A.-F. A. Trompeta, I. G. Aviziotis, and C. A. Charitidis, "Unraveling the mechanisms of carbon nanotube growth by chemical vapor deposition," *Chem. Eng. J.*, vol. 445, p. 136807, Oct. 2022, doi: 10.1016/j.cej.2022.136807.
[28] V. Jourdain and C. Bichara, "Current understanding of the growth of carbon nanotubes in catalytic chemical vapour deposition," *Carbon*, vol. 58, pp. 2–39, Jul. 2013, doi: 10.1016/j.carbon.2013.02.046.
[29] Z. Bian, S. Das, M. H. Wai, P. Hongmanorom, and S. Kawi, "A Review on Bimetallic Nickel-Based Catalysts for CO_2 Reforming of Methane," *ChemPhysChem*, vol. 18, no. 22, pp. 3117–3134, Nov. 2017, doi: 10.1002/cphc.201700529.
[30] C. J. Lee, J. Park, and J. A. Yu, "Catalyst effect on carbon nanotubes synthesized by thermal chemical vapor deposition," *Chem. Phys. Lett.*, vol. 360, no. 3–4, pp. 250–255, Jul. 2002, doi: 10.1016/S0009-2614(02)00831-X.
[31] Z. P. Huang, D. Z. Wang, J. G. Wen, M. Sennett, H. Gibson, and Z. F. Ren, "Effect of nickel, iron and cobalt on growth of aligned carbon nanotubes," *Appl. Phys. Mater. Sci. Process.*, vol. 74, no. 3, pp. 387–391, Mar. 2002, doi: 10.1007/s003390101186.
[32] S. A. Moshkalyov, A. L. D. Moreau, H. R. Guttiérrez, M. A. Cotta, and J. W. Swart, "Carbon nanotubes growth by chemical vapor deposition using thin film nickel catalyst," *Mater. Sci. Eng. B*, vol. 112, no. 2–3, pp. 147–153, Sep. 2004, doi: 10.1016/j.mseb.2004.05.038.

[33] C. Lei, F. Markoulidis, Z. Ashitaka, and C. Lekakou, “Reduction of porous carbon/Al contact resistance for an electric double-layer capacitor (EDLC),” *Electrochimica Acta*, vol. 92, pp. 183–187, Mar. 2013, doi: 10.1016/j.electacta.2012.12.092.
[34] H.-C. Wu *et al.*, “High-performance carbon-based supercapacitors using Al current-collector with conformal carbon coating,” *Mater. Chem. Phys.*, vol. 117, no. 1, pp. 294–300, Sep. 2009, doi: 10.1016/j.matchemphys.2009.06.001.
[35] Y. Gogotsi and R. M. Penner, “Energy Storage in Nanomaterials – Capacitive, Pseudocapacitive, or Battery-like?,” *ACS Nano*, vol. 12, no. 3, pp. 2081–2083, Mar. 2018, doi: 10.1021/acsnano.8b01914.
[36] K. DU, X. CHEN, and P. A. ØHLCKERS, “DIRECT GROWTH CROSS-LINKED CARBON NANOTUBES ON MICROSTRUCTURED METAL SUBSTRATE FOR SUPERCAPACITOR APPLICATION,” WO 2022/078759 A1, Apr. 21, 2022
[37] R. T. K. Baker, “Catalytic growth of carbon filaments,” *Carbon*, vol. 27, no. 3, pp. 315–323, 1989, doi: 10.1016/0008-6223(89)90062-6.
[38] S. Amelinckx, X. B. Zhang, D. Bernaerts, X. F. Zhang, V. Ivanov, and J. B. Nagy, “A Formation Mechanism for Catalytically Grown Helix-Shaped Graphite Nanotubes,” *Science*, vol. 265, no. 5172, pp. 635–639, Jul. 1994, doi: 10.1126/science.265.5172.635.
[39] V. Popov, “Carbon nanotubes: properties and application,” *Mater. Sci. Eng. R Rep.*, vol. 43, no. 3, pp. 61–102, Jan. 2004, doi: 10.1016/j.mser.2003.10.001.
[40] A. Huczko, “Synthesis of aligned carbon nanotubes,” *Appl. Phys. Mater. Sci. Process.*, vol. 74, no. 5, pp. 617–638, May 2002, doi: 10.1007/s003390100929.
[41] M. V. Kharlamova, “Investigation of growth dynamics of carbon nanotubes,” *Beilstein J. Nanotechnol.*, vol. 8, pp. 826–856, Apr. 2017, doi: 10.3762/bjnano.8.85.
[42] R. Xiang *et al.*, “Growth Deceleration of Vertically Aligned Carbon Nanotube Arrays: Catalyst Deactivation or Feedstock Diffusion Controlled?,” *J. Phys. Chem. C*, vol. 112, no. 13, pp. 4892–4896, Apr. 2008, doi: 10.1021/jp710730x.
[43] M. N. Chaudhari, “Thin film Deposition Methods: A Critical Review,” *Int. J. Res. Appl. Sci. Eng. Technol.*, vol. 9, no. VI, pp. 5215–5232, Jun. 2021, doi: 10.22214/ijraset.2021.36154.
[44] M. Ohring, *The Materials Science of Thin Films*, 2nd ed. Academic Press.
[45] D. Lundin, “Plasma properties in high power impulse magnetron sputtering,” Linköping Studies in Science and Technology, SE-581 83 Linköping, Sweden, 2008.
[46] S. A. Chang, M. B. Skolnik, and C. Altman, “High rate sputtering deposition of nickel using dc magnetron mode,” *J. Vac. Sci. Technol. Vac. Surf. Films*, vol. 4, no. 3, pp. 413–416, May 1986, doi: 10.1116/1.573893.
[47] I. V. Tudose *et al.*, “Chemical and physical methods for multifunctional nanostructured interface fabrication,” in *Functional Nanostructured Interfaces for Environmental and Biomedical Applications*, Elsevier, 2019, pp. 15–26. doi: 10.1016/B978-0-12-814401-5.00002-5.
[48] G. F. Iriarte, J. G. Rodríguez, and F. Calle, “Synthesis of c-axis oriented AlN thin films on different substrates: A review,” *Mater. Res. Bull.*, vol. 45, no. 9, pp. 1039–1045, Sep. 2010, doi: 10.1016/j.materresbull.2010.05.035.
[49] A. Zendehnam, M. Ghanati, and M. Mirzaei, “Study and comparison of deposition rates, grain size of Ag and Cu thin films with respect to sputtering parameters, and annealing temperature,” *J. Phys. Conf. Ser.*, vol. 61, pp. 1322–1325, Apr. 2007, doi: 10.1088/1742-6596/61/1/261.

[50] B. Geetha Priyadarshini, S. Aich, and M. Chakraborty, “Structural and morphological investigations on DC-magnetron-sputtered nickel films deposited on Si (100),” *J. Mater. Sci.*, vol. 46, no. 9, pp. 2860–2873, May 2011, doi: 10.1007/s10853-010-5160-6.
[51] G. F. Iriarte, J. G. Rodriguez, and F. Calle, “Effect of substrate–target distance and sputtering pressure in the synthesis of AlN thin films,” *Microsyst. Technol.*, vol. 17, no. 3, pp. 381–386, Mar. 2011, doi: 10.1007/s00542-010-1198-2.
[52] G. F. Iriarte, F. Engelmark, and I. V. Katardjiev, “Reactive Sputter Deposition of Highly Oriented AlN Films at Room Temperature,” *J. Mater. Res.*, vol. 17, no. 6, pp. 1469–1475, Jun. 2002, doi: 10.1557/JMR.2002.0218.
[53] “Scanning Electron Microscopy (SEM).” https://serc.carleton.edu/research_education/geochemsheets/techniques/SEM.html
[54] M. Hirasawa, H. Shirakawa, H. Hamamura, Y. Egashira, and H. Komiyama, “Growth mechanism of nanoparticles prepared by radio frequency sputtering,” *J. Appl. Phys.*, vol. 82, no. 3, pp. 1404–1407, Aug. 1997, doi: 10.1063/1.365917.
[55] M. Vopsaroiu, M. J. Thwaites, S. Rand, P. J. Grundy, and K. O’Grady, “Novel Sputtering Technology for Grain-Size Control,” *IEEE Trans. Magn.*, vol. 40, no. 4, pp. 2443–2445, Jul. 2004, doi: 10.1109/TMAG.2004.828971.
[56] A. Sharma, S. Mohan, and S. Suwas, “The influence of deposition temperature on the structure, microstructure, morphology and magnetic properties of sputter deposited nickel thin films,” *Thin Solid Films*, vol. 619, pp. 91–101, Nov. 2016, doi: 10.1016/j.tsf.2016.10.024.

Appendix

ImageJ analysis of Ni thin film 100 nm 100W for cluster diameter measurement pre and post heat treatment.

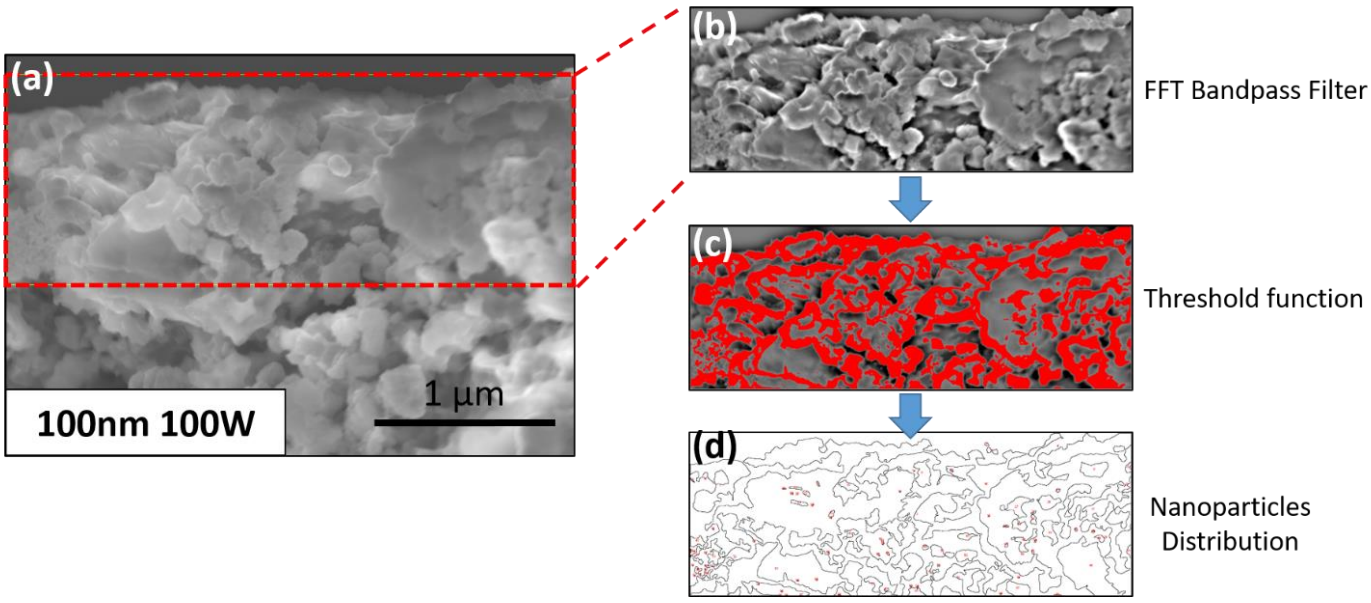

Figure 46: ***(a)*** *area selection,* ***(b)*** *FFT bandpass filter,* ***(c)*** *threshold function,* ***(d)*** *nanoparticles dsitribution.*

Table 10: Thin film - 100 nm 100 W - comparison of Ni cluster diameter before and after heat treatment shows an increase in the diameter.

Power (W)	Before Heating : Ni Cluster Diameter (nm)	After Heating : Ni Clusters Diameter (nm)
100	79.8	138.23